Journal of Volcanology and Geothermal Research 455 (2024) 108159

Contents lists available at ScienceDirect

Journal of Volcanology and Geothermal Research

journal homepage: www.journals.elsevier.com/journal-of-volcanology-and-geothermal-research

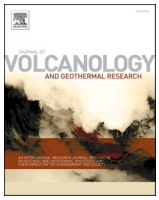

The rheology of rhyolite magma from the IDDP-1 borehole and Hrafntinnuhryggur (Krafla, Iceland) with implications for geothermal drilling

Fabian B. Wadsworth [a,*], Jérémie Vasseur [b], Yan Lavallée [b], Kai-Uwe Hess [b], Jackie E. Kendrick [b], Jonathan M. Castro [c], Daniel Weidendorfer [b], Shane M. Rooyakkers [d], Annabelle Foster [a], Lucy E. Jackson [a], Ben M. Kennedy [e], Alexander R.L. Nichols [e], C. Ian Schipper [f], Bettina Scheu [b], Donald B. Dingwell [b], Tamiko Watson [e], Georgina Rule [e], Taylor Witcher [g], Hugh Tuffen [h]

[a] Department of Earth Sciences, Durham University, DH1 3LE, UK
[b] Earth and Environmental Sciences, Ludwig-Maximilians-Universität München, 80333 Munich, Germany
[c] Institute of Geosciences, Johannes Gutenberg University, Mainz, Germany
[d] GNS Science, Lower Hutt 5011, New Zealand
[e] School of Earth and Environment, Te Kura Aronukurangi, University of Canterbury, Te Whare Wānaga o Waitaha, Private Bag 4800, Christchurch, Ōtautahi 8140, New Zealand
[f] School of Geography, Environment, and Earth Sciences, Te Herenga Waka, Victoria University of Wellington, PO Box 600, Wellington 6140, New Zealand
[g] Department of Earth Sciences, Uppsala University, Villavägen, 16 75236 Uppsala, Sweden
[h] Lancaster Environment Centre, Lancaster University, Lancaster, United Kingdom

ARTICLE INFO

Keywords:
Viscosity
Silicic eruption
Obsidian
Magma
Volcanic eruption
Rhyolite
Relaxation

ABSTRACT

Changes in rhyolite melt viscosity during magma decompression and degassing exert a first order control on ascent through the crust and volcanic eruption style. These changes have as yet unknown hazard implications for geothermal drilling in pursuit of particularly hot fluids close to magma storage regions. Here, we exploit the situation at Krafla volcano in which rhyolite has both erupted at Earth's surface and been sampled at shallow storage depths via drilling of the 2009 IDDP-1 and 2008 KJ-39 boreholes. We use differential scanning calorimetry to constrain that the IDDP-1 magma quenched to glass at ~ 700 K, at a rate of between 7 and 80 K.min^{-1}. We measure the equilibrium viscosity of the IDDP-1 rhyolite at temperatures close to the glass transition interval and show that the rhyolite viscosity is consistent with generalized viscosity models assuming a dissolved H_2O concentration of 2.12 wt%. We couple these results with micro-penetration and concentric cylinder rheometry over a range of potential magma storage temperatures to constrain the response of surficial Krafla rhyolites to stress. The surficial rhyolites at Krafla match the same viscosity model, assuming a lower dissolved H_2O concentration of 0.12 wt%. Our results show that at a storage temperature of 1123–1193 K, the viscosity of the stored magma is ~ 3×10^5 Pa.s. At the same temperature, the viscosity following degassing during ascent to the surface rises to ~ 2×10^9 Pa.s. Finally, we use high-stress compression tests on the Hrafntinnuhryggur surface obsidian to determine the onset of unrelaxed behavior and viscoelastic melt rupture or fragmentation pertinent to understanding the melt response to rapid pressure changes that may be associated with further (near-) magma exploration at Krafla. Taken together, we characterize the relaxation and viscosity of these magmas from source-to-surface.

1. Introduction

The rheology of magmatic liquids exerts a first order control on whether or not a volcanic eruption will be explosive (e.g., Cassidy et al., 2018). Part of the challenge for Earth scientists is to decipher the ways in which rheology evolves during magma ascent through the crust. Physical and chemical processes such as bubble growth (Sparks, 1978; Blower et al., 2001; Coumans et al., 2020), crystallization (e.g. La Spina

* Corresponding author.
E-mail address: fabian.wadsworth@gmail.com (F.B. Wadsworth).

https://doi.org/10.1016/j.jvolgeores.2024.108159
Received 14 May 2024; Received in revised form 24 July 2024; Accepted 1 August 2024
Available online 2 August 2024

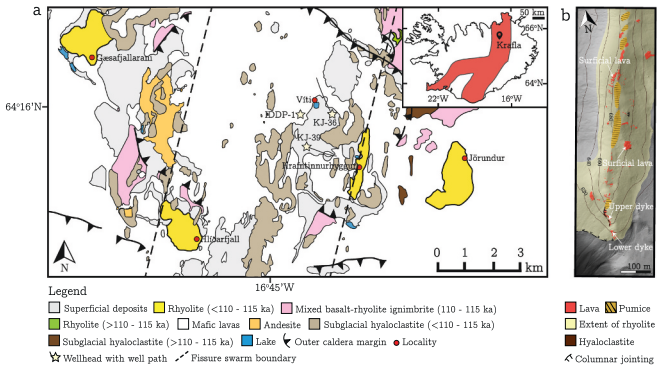

Fig. 1. (a) Map of the Krafla volcanic field (Iceland) showing the location of the Hrafntinnuhryggur rhyolite, the 2009 IDDP-1 borehole well head (drilled approximately vertically), and the KJ-39 borehole well head (including the slanted projection of the inclined borehole). Additionally shown are other Krafla rhyolites: Víti, Jörundur, Hlíðarfjall, and Gæsafjallarani. *Inset*: the location of Krafla in the wider Icelandic rift zone(s). This map is simplified from a published source (Sæmundsson et al., 2012). (b) An annotated digital elevation model of the Hrafntinnuhryggur ridgeline adapted from Foster et al. (2024) and showing the surficial lava, pumice, and hyaloclastite (country rock) outcrops.

et al., 2021), flash nanolitisation (Di Genova et al., 2020; Cáceres et al., 2020; Pereira et al., 2024), and temperature changes due to cooling (including latent heat effects; Blundy et al., 2006), viscous dissipation as heat, or friction (Mastin, 2005; Petcovic and Dufek, 2005; Costa et al., 2007; Lavallée et al., 2015a; Kendrick and Lavallée, 2022), all lead to rheological changes in the melt phase and feedback with the variable development of multiphase suspension rheology (Mader et al., 2013). A standard approach to understanding melt rheology has been to determine the equilibrium viscosity of melts in the laboratory at relevant magmatic conditions and to use these measurements to calibrate empirical model fits. This approach is underpinned by the range of conditions over which the rheological determinations have now been made, encompassing much of the breadth of temperature and dissolved volatile concentrations extant in magmas in the upper crust (Hess and Dingwell, 1996; Giordano et al., 2008), and exemplified by the low relative residuals between experimental observations and models. However, in most cases, only volcanic deposits at the Earth's surface are directly accessible, and so there remains a degree of uncertainty in the application of these constitutive rheological models to magma transport and eruption.

Drilling projects such as the Iceland Deep Drilling Project (IDDP) afford an opportunity to access and sample the sub-surface directly. The IDDP-1 borehole was drilled approximately vertically in 2009 at Krafla volcano and was designed to reach 4–5 km below the surface in pursuit of supercritical fluids associated with magmatic intrusions. However, at 2.1 km depth, the drill intercepted rhyolitic magma, evidenced by the appearance of quenched silicic glass chips in the drill cuttings (Friðleifsson et al. 2010; Elders et al., 2011). The borehole assembly was pushed upward for 4 min, before the melt was fully quenched by drilling fluid, and became stuck (Friðleifsson et al. 2010; Pálsson et al., 2014). This interception of rhyolitic melt and direct sampling of quenched silicic glass from depth provides a unique opportunity to study a shallow rhyolitic magma in situ (Eichelberger, 2019; Saubin et al., 2021), as well as demonstrating the production potential associated with high-temperature fluids (Ingason et al., 2014). Importantly, there are surface effusive rhyolites exposed within ~2 km of the IDDP-1 drill site (Fig. 1) at Krafla (Jónasson, 1994; Tuffen and Castro, 2009; Rooyakkers et al., 2021b), offering a chance to study compositionally similar rhyolites in both a pre- and post-eruptive state.

Prior to the well-known IDDP-1 borehole, the KJ-39 borehole was drilled in 2008, south of the Leibortnar-Vítismór field and ~2.5 km south of IDDP-1 (Fig. 1). This was drilled directionally to the east at an angle of 30° from vertical with the same aim as IDDP-1: to access supercritical fluids for geothermal purposes. The drill string reached a maximum down-hole distance of 2.865 km where it was stuck and, after being freed using explosives, the bottom hole assembly was found to contain drill cuttings including quenched silicic glass. This, together with the high down-hole temperatures in excess of the local geotherm, the silicic glass suggested that the hole had intersected magma (Mortensen et al., 2010; Rule, 2020). Therefore, there are two candidate case studies of deep silicic glass extraction from shallow storage regions at Krafla volcano: KJ-39 and IDDP-1.

Here, motivated by the need to better understand magma properties and potential response to future (in-situ/near-) magma drilling efforts, such as envisaged in the Krafla Magma Testbed (KMT: see https://www.kmt.is/; Eichelberger, 2019; Lavallée et al. *in review*), we constrain the rheology of silicic magmatic liquids in a case-study location where both the stored magma and an erupted equivalent of the same rhyolitic magma can be studied in tandem. These rheological data will inform ongoing and future efforts aiming at modelling the potential response of magma to drilling, thus supporting implementation plans and risk mitigation strategies for such endeavors.

2. Materials: Hrafntinnuhryggur and IDDP-1

We use rhyolitic glass from two neighboring sites in the Krafla volcanic system: Hrafntinnuhryggur ('obsidian ridge') and the IDDP-1 borehole (Fig. 1). In both cases the glass is taken to represent the melt phase typical of either system (surface and 2.1 km borehole depth, respectively). While these rhyolites are not thought to be genetically linked, they have similar compositions (Table 1; Tuffen and Castro,

Table 1
Average renormalized composition of IDDP-1 and Hrafntinnuhryggur.

Oxide*	IDDP-1 ($n = 295$)	Standard deviation	Hrafntinnuhryggur ($n = 15$)	Standard deviation
SiO_2	77.02	2.81	75.03	0.35
TiO_2	0.3	0.07	0.24	0.02
Al_2O_3	11.78	1.44	12.33	0.18
$FeO_{(T)}$**	2.68	0.56	3.25	0.19
MnO	0.07	0.03	0.14	0.04
MgO	0.19	0.07	0.09	0.02
CaO	1.32	0.44	1.69	0.06
Na_2O	3.33	0.43	4.48	0.19
K_2O	3.31	0.83	2.75	0.08
Mol. fraction excess cations#	0.0256		0.0387	
Anhydrous shift factor, c (Pa.K)+	1.43×10^{10}		1.21×10^{10}	
Reference sources	Zierenberg et al. (2013); Masotta et al. (2018); Saubin et al. (2021)		Tuffen and Castro (2009); Rooyakkers et al. (2021a, 2021b)	

* Composition is renormalized to 100% total on an anhydrous basis after taking the average for each oxide.
** All iron is assumed to be FeO.
\# Cations excess to charge balancing roles.
\+ Computed via Gottsmann et al. (2002).

2009; Hampton et al., 2021; Saubin et al., 2021; Rooyakkers et al., 2021b), overlapping values of $\delta^{18}O$ (IDDP-1: 3.1‰, Hrafntinnuhryggur: 2.92–3.28 ‰; Hampton et al., 2021), and a similar proposed petrogenesis. The differences in composition are subtle in the context of the influence of compositional differences on properties such as viscosity (Hess et al., 1995). In the context of rheological properties, the key difference between the two materials is the dissolved concentration of volatiles, predominantly H_2O. On petrogenetic grounds, a more appropriate direct choice for the surface expression material might have been the recent rhyolitic eruptive products from the Víti crater (Rooyakkers et al., 2021a), however, this material is not as readily available in large glassy chunks such as at Hrafntinnuhryggur for large scale testing. The opportunity for sampling large, broadly homogeneous pieces of the Hrafntinnuhryggur obsidian, facilitates the multi-method rheological tests that we deploy here. For these reasons, we use the Hrafntinnuhryggur obsidian as a proxy for a surface expression of the IDDP-1 rhyolite encountered during drilling.

2.1. Hrafntinnuhryggur obsidian

The ~24 ka Hrafntinnuhryggur ridge (eruption age from Sæmundsson et al., 2000) represents a shallow intrusive-to-extrusive rhyolite exposure, extending down to a maximum of 95 m below the paleo-surface (Tuffen and Castro, 2009; Tuffen et al., 2010; Saubin et al., 2019; Foster et al., 2024). The rhyolitic surface outcrops (not including the feeder dyke outcrops) at Hrafntinnuhryggur include obsidian-dominated and devitrified-rhyolite-dominated facies (Castro et al., 2009; Tuffen and Castro, 2009). We used the obsidian as our experimental material throughout (note that the devitrified rhyolite is thought to be the crystallized counterpart of the obsidian).

Across all lithofacies outcropping at Hrafntinnuhryggur, the total dissolved H_2O concentration in the obsidian was measured previously by Fourier transform infrared spectroscopy (FTIR) to be between 0.11 ± 0.01 (sample OR1605) and 0.20 ± 0.01 (sample OR1705) in wt% (Tuffen and Castro, 2009), where we have converted standard deviation to standard error using the quoted number of analyses per sample. Also using FTIR on obsidian from one section of the Hrafntinnuhryggur site, Ryan et al. (2015a, 2015b) measured the H_2O concentration to be 0.11 ± 0.04 wt%, Seropian et al. (2022) measured 0.11 ± 0.01 wt%, and Weaver et al. (2023) measured 0.10 ± 0.01 wt%. These ranges of H_2O concentrations are broadly consistent with constraints by thermogravimetric analysis in which the bulk mass loss up to a high temperature of 1375 K is assumed to represent a volatile concentration in excess of the solubility at those same temperatures at low partial H_2O pressures of laboratory conditions. Using this method and assuming the volatiles are dominated by H_2O, Wadsworth et al. (2018) and Wadsworth et al. (2019) found 0.14 ± 0.03 wt%, and 0.15 ± 0.03 wt% H_2O, (respectively)

2.2. IDDP-1 borehole rhyolite

In the case of IDDP-1, chips of both obsidian and felsite were recovered during drilling. Following previous work, we interpret the obsidian chips as representing the quenched product of the melt stored at depth at Krafla. The obsidian chips were all rhyolitic (Fig. 2) and contained minor crystallinity (mostly <3 vol%), consisting of small, <100 μm, crystals of pyroxene, titanomagnetite, and plagioclase (Elders et al., 2011; Zierenberg et al., 2013; Masotta et al., 2018; Saubin et al., 2021). Rare chips containing high crystallinity (55–100 vol%) are inferred to reflect partial melting of the host felsite (Zierenberg et al., 2013; Masotta et al., 2018), so are not considered here in the context of magma rheology. Typical glass chip internal textures are shown in **Fig. 3**. The dissolved volatile fractions measured previously on these materials are 1.29–2.15 wt.% H_2O (with outlier individual analyses at 0.09 and 3.42 wt.%) and a CO_2 concentration on the order of 100 ppm (Elders et al., 2011; Zierenberg et al., 2013; Lowenstern and Pitcher,

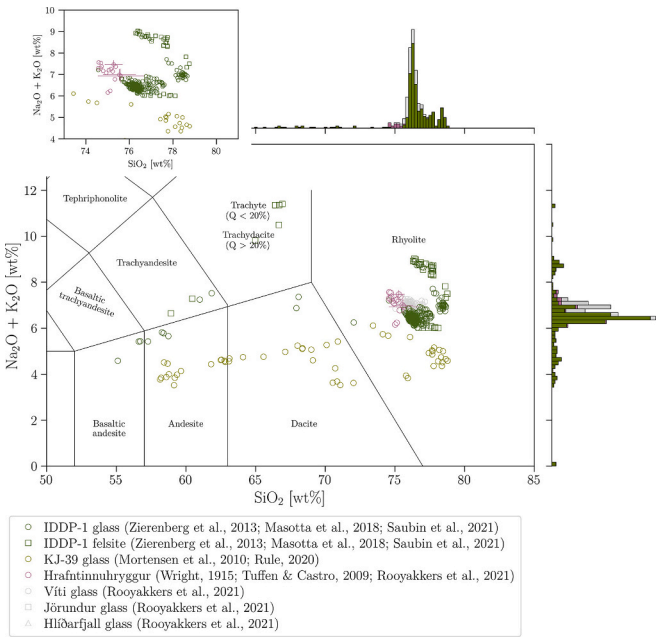

Fig. 2. Total-alkali-silica (TAS) plot showing the glass and melt inclusion data available for the rhyolites and borehole glass chips relevant to this study from published sources (Wright, 1915; Tuffen and Castro, 2009; Mortensen et al., 2010; Zierenberg et al., 2013; Masotta et al., 2018; Rule, 2020; Saubin et al., 2021; Rooyakkers et al., 2021b). *Inset:* a zoom-in of the main plot restricted to the rhyolite field and only showing the Hrafntinnuhryggur and IDDP-1 datasets, for clarity.

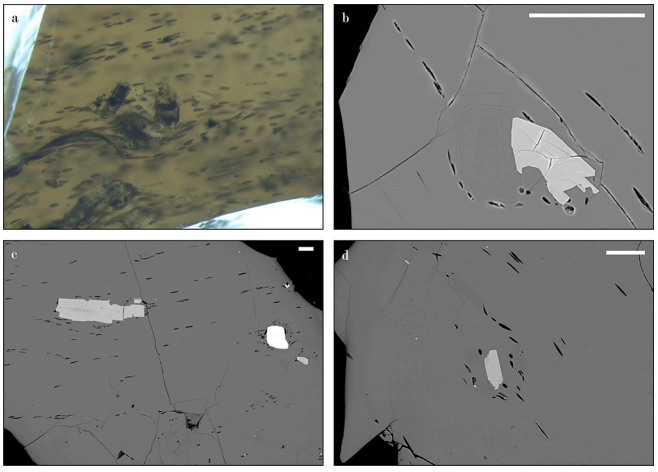

Fig. 3. Images of the IDDP-1 glass chip textures. (a) A photomicrograph taken using a binocular microscope and showing deformed vesicles deflected around a local concentration of crystals with a horizontal field of view of 1.6 mm. (b-d) Backscattered electron images showing phenocrysts, groundmass glass, and deformed vesicles. The white scale bar represents 100 μm.

2013; Watson, 2018; Bindeman et al., 2021; Saubin et al., 2021). There is no evidence of magma chemical interaction with the drilling fluids, such as hydration, because the measured OH/H_2O ratio is 1.46–2.53 (Zierenberg et al., 2013). Additionally, no evidence for hydrated margins of individual chips were found in FTIR transects (Watson, 2018). Two-pyroxene geothermometry and modelling of the crystallization sequence suggests in situ storage melt temperature of 1123–1193 K (Zierenberg et al., 2013).

2.3. The Hrafntinnuhryggur feeder dyke system

The Hrafntinnuhryggur lavas described briefly in Section 2a lie stratigraphically above an intrusive obsidian-dominated rhyolite dyke that is exposed at two depths below the paleo-surface: approximately 35–50 m and 95 m (Tuffen et al., 2010; Saubin et al., 2019; Foster et al., 2024). FTIR analyses show that these intrusions have variable H_2O concentrations in the range 0.32–0.53 wt% (Tuffen and Castro, 2009; Tuffen et al., 2010; Foster et al., 2024). These outcrops are inferred to represent a shallow conduit region that experienced less degassing than the surface outcrops.

3. Analytical and synthesis methods

We supplement the H_2O concentration analyses of those measured in the Hrafntinnuhryggur feeder dyke system with new measurements using a ThermoScientific™ FlashSmart™ elemental analyzer which employs a modified Dumas method. Glass chips (2–5 mg) are enclosed in tin containers and combusted in the presence of high purity oxygen with helium as a carrier gas. The combustion products in the gas stream are carried to a gas chromatograph where hydrogen is detected by thermal conductivity and then recalculated to a weight percentage of H_2O using the initial sample mass as a total, and the assumption of complete combustion. This device was calibrated using a BBOT standard and verified with secondary standards before and after measuring each sample. Further details pertaining to this method are provided elsewhere (Moussallam et al., 2016; Weidendorfer et al., 2023).

In order to calibrate our thermal analysis methods and the manner in which they can reveal information about the viscosity of melts (discussed in Section 4), we synthesize a small aliquot of obsidian with 2 wt % H_2O. To do this, we place 151 mg of powdered obsidian from Hrafntinnuhryggur along with 3.1 mg of distilled water into a 14 mm long Au capsule (4.0 mm outer diameter, 3.6 mm inner diameter) and seal it shut using a PUK micro-welding system. Then the capsule is loaded into a rapid-quench molybdenum-hafnium-carbide (MHC) cold-seal apparatus. The sample is compressed to 150 MPa using Ar gas as pressure medium before heating the experimental charge to 1273.15 K at a constant heating rate of 15 K/min. We hold the capsule at those pressure–temperature conditions for 17.5 hours before quenching the run isobarically. The resultant synthesized sample is a natural obsidian but hydrated with 2 wt% H_2O. This sample is referred to later as the 'hydrated obsidian'.

4. Experimental methods

Our experimental methods involved: (1) thermal analysis and (2) rheological determination. The aim of the first approach is to constrain the structural relaxation behavior of both the Hrafntinnuhryggur glassy lavas and the IDDP-1 glass chips upon heating. The aim of the second approach is to constrain the rheology of the obsidian lavas at Hrafntinnuhryggur. By using existing validated frameworks for silicate melt relaxation dynamics, we can then unify these two approaches and constrain the rheology of the glass at storage conditions intercepted by IDDP-1, and at the Earth's surface. This workflow is described here.

4.1. Rheology via thermal analysis using differential scanning calorimetry

We use a Netzsch GmbH Pegasus 404c differential scanning calorimeter to constrain the glass transition temperature (as a function of heating or cooling rate) and gain an approximate constraint of the natural cooling rate of the glass samples (Wilding et al., 1996; Gottsmann et al., 2002). We use 30–50 mg chunks of glass loaded into a lidded platinum-rhodium crucible. The crucible is heated in argon or in air at constant rates of heating. The measurement consists of the heat flow (recorded as a voltage in a thermocouple array) at the base of the sample crucible relative to at the base of an empty reference crucible. We perform runs with new samples; first we heated them at 25 K.min^{-1} to a temperature of 823 K (in the case of the IDDP-1 samples) and 1123 K (in the case of the Hrafntinnuhryggur obsidian), causing relaxation of the glass and eradication of the thermal history associated with cooling in nature or during drilling. Subsequently we cool the sample at a given rate (e.g., 5, 10, 25 K.min^{-1}) to vitrify the melt and impose a given structural configuration of the glass at a known rate, before heating it again at the same rate to evaluate the glass transition under that matched pair of cooling/heating rates. Then this is repeated at different cooling/heating rate pairs to map shifts in the glass transition under a range of rates. This thermal analysis allows us to find the onset and the peak of the glass transition interval below which the glass is a solid and above which the glass can relax applied stresses viscously. In all cases, we subtract a best-fit baseline (applied to temperatures below the glass transition) from the heat flow data. To do this, we look by eye for the heat flow data that is clearly prior (in temperature) to the onset of the glass transition and fit a polynomial of the form $\beta = d_1 T^{-1} + d_2 T^{-2} + d_3$ (Maier and Kelley, 1932) to the data, where β is the heat flow (in arbitrary units), T is the temperature, and d_1, d_2 and d_3 are fit constants. We then subtract this best-fit function from the data in order to render the heat flow curve flat ('baseline subtracted') prior to the glass transition.

The technique of matched cooling-heating runs allows us to observe the dependence of the glass transition on the rate of temperature change (Wilding et al., 1996; Gottsmann et al., 2002), using the semi-empirical relation

$$\mu|_{T_g} = \frac{c}{|q|} \tag{1}$$

where $\mu|_{T_g}$ is the viscosity assessed at the glass transition temperature T_g, $|q|$ is the absolute value of the heating or cooling rate q, and c is a constant (with units of Pa.K) that relates the viscosity to its imposed prior cooling and re-heating history (sometimes referred to as a 'shift factor'). c is a weak function of glass composition, and there exists an empirical calibration that relates c to the mol.% cations in the melt that are excess to the charge balancing roles $\mathscr{X}$ dictated by the network-forming cations (Gottsmann et al., 2002). This empirical model is $c = 10.321 - 0.175\ln(\mathscr{X})$.

For the average of the Hrafntinnuhryggur and IDDP-1 compositions given in Fig. 2 (see Table 1), we find that $c \approx 1.21 \times 10^{10}$ Pa.K and $c \approx 1.43 \times 10^{10}$ Pa.K, respectively. These values are found via $\mathscr{X}$ with zero H_2O accommodated in the calculation (i.e., anhydrous compositions); this is discussed later in Section 5). To arrive at these values, we assume that the net effect of iron is not substantial, given that whatever oxidation state we assume (partitioning iron into FeO and Fe_2O_3), the contribution of iron to $\mathscr{X}$ is negligible.

4.2. Relaxation geospeedometry using differential scanning calorimetry

In silicate glasses, a given property p (such as shear stress) will relax with time proportional to a characteristic relaxation time λ. A common constitutive relaxation equation is the Kohlrausch-Williams-Watts function $p = p_0 \exp[-(t/\lambda)^{\zeta}]$ where p_0 is the initial value of p prior to relaxation (such as the applied stress), t is time since the onset of relaxation, and ζ is an exponent that, when $\zeta < 1$, stretches the relaxation function beyond a simple exponential, and which is often required to fit data (Kohlrausch, 1854; Williams and Watts, 1970; Debolt et al., 1976; Kenderes and Whittington, 2021). The propensity for glasses to relax a given property underpins the idea behind relaxation geospeedometry in which the functional shape of the evolution of the heat capacity across the glass transition is dictated by the enthalpy relaxation path taken by the glass (Debolt et al., 1976). Because the heat capacity evolution at a given heating rate is dictated by the cooling rate at which the glass was formed, models for heat capacity evolution can be used to extract the cooling rate at which glass forms. The theoretical underpinning of this model is described elsewhere (Debolt et al., 1976; Hodge,

2008) and so here we simply introduce the procedural methodology for extracting the cooling rate at which glass – including natural glass – forms.

The fictive temperature T' is the temperature at which the molecular structure of a glass was in equilibrium. At high temperatures far in excess of the glass transition T_g, the fictive temperature and the absolute temperature are equal $T' = T$. If a glass is cooled at a constant rate from the condition that $T' = T$, then at a certain temperature, the glass structure will cease to be in equilibrium because the structure becomes relaxation-limited. A functional model for T' is (Debolt et al., 1976)

$$T' = T_0 + \sum_{j=1}^{m} \left(T'_{(j-1)} - T_{(j)} \right) \left(1 - \exp\left[- \left(\sum_{k=j}^{m} \frac{T_{(k)} - T_{(k-1)}}{q\lambda_{(k)}} \right)^{\zeta} \right] \right) \quad (2)$$

where T_0 is a temperature far from T_g, j is the index of the iteration being performed in Eq. (2), q is the cooling or heating rate, $\lambda_{(k)}$ is the relaxation timescale at index k (i.e., at a given temperature step) and m is the final step. In practice, this is a sum, as shown in Eq. (2), but more properly is an integration procedure. $\lambda_{(k)}$ is given by

$$\lambda_{(k)} = \lambda_0 \exp\left[s\frac{\Delta H}{RT_{(k)}} + (1-s)\frac{\Delta H}{RT'_{(k-1)}} \right] \quad (3)$$

where λ_0 and s are fit parameters with $0 < s < 1$ bounds. ΔH is the enthalpy of relaxation. Here R is the universal gas constant. In order to convert Eq. (2) to a heat flow signal, we use

$$\frac{dT}{dt} = \frac{\beta - \beta_g}{\beta_l - \beta_g} \quad (4)$$

where β is the heat flow signal, β_g is the heat flow signal in the glass (given by the baseline normalization introduced in Section 4a), and β_l is the constant high-temperature heat flow signal for the melt.

Procedurally, we use differential scanning calorimetry (introduced in Section 4a) to record the heat flow signal across the glass transition (which is a proxy for the heat capacity). First, we load a sample that was cooled at an unknown rate termed the 'natural' cooling rate, and heat it at a known heating rate. This produces a signal that we must model using Eqs. (2 & 3) in order to predict the cooling rate at which the glass was originally formed in nature or during drilling. However, for a given glass, ζ, s, ΔH, and λ_0 are all unknowns that depend on glass composition only (Kenderes and Whittington, 2021). Therefore, once the natural signal is obtained, we then heat and cool the samples at known matched cooling-heating rates, cycling through the glass transition window. By doing this, we set q in Eq. (2) to a given value that is the case on both the cooling and the subsequent heating cycle. We then minimize using a least-squares regression (Kemmer and Keller, 2010) for the fit parameters ζ, s, and λ_0. We find ΔH by acknowledging $-\ln q = -\ln q_0 + \Delta H/(RT_g)$,[1] where q_0 is a fit parameter intercept[2] in a plot of the peak glass transition temperature T_g from the signal as a function of q. Once the fit parameters are determined, the 'natural' curve signal can then be fit with only one fit parameter that is q on cooling.

4.3. Rheological determination

We use a combination of methods to determine the rheology of natural obsidian from Hrafntinnuhryggur that, taken together, cover a wide range of applied temperatures and shear stresses. The aim of this multi-method approach is to build a full picture of the melt behavior across all conditions extant in shallow magma transport and eruption.

First, to determine the viscosity at relatively high temperatures, we use a rotational rheometer in which crushed chips of each raw glass are loaded into thin-walled platinum crucibles and stirred at 1773 K for 24 hours, using a $Pt_{80}Rh_{20}$ spindle to homogenize and remove bubbles. The samples are then removed from the thin-walled synthesis crucible by drilling and hammering. The resulting chips are transferred to a thick walled $Pt_{80}Rh_{20}$ viscometry crucible of exact geometry and stirred again to ensure homogenization and an absence of bubbles. A $Pt_{80}Rh_{20}$ viscometry spindle (Dingwell and Virgo, 1988) is immersed in the melt and controlled using a Brookfield viscometer which operated at rotation speeds of 0.1–40 rpm. The apparatus, technique, and data processing are described by Dingwell (1989). The technique involves a series of temperature reduction steps with dwells of 1 h to ensure the system equilibrates thermally, yielding constant torque. The equilibrium torque is then proportional to the shear stress, which is used with the rotation rate to compute the shear viscosity.

At lower temperatures, just above the glass transition interval, we apply the micro-penetration technique (Hess et al., 1995). This involves determining the rate at which a hemispherical iridium indenter displaces the melt when a fixed load is applied. These measurements are applied to the obsidian, cut into 3 mm long plane-parallel discs 5 mm in diameter and polished on both surfaces. The sample is placed in a Netzsch GmbH 402 F1/F3 Hyperion thermo-mechanical analyzer under argon gas flow and the indenter is attached to the vertical push rod. The viscosity is then determined from $\mu = \gamma Ft\left(\xi\alpha^3\right)^{-1/2}$ where $\gamma = 0.1875$ is a dimensionless constant for a hemispherical indenter, F is the applied force, t is the time since contact of the indenter, ξ is the indenter radius (1 mm in this case) and α is the time dependent distance into the silicate liquid (Pocklington, 1940; Tobolsky and Taylor, 1963). The viscosity μ is taken at steady-state (high values of t at which $d\alpha/dt$ becomes constant).

In addition, we can access the relatively low-temperature end of the viscosity spectrum using cylinder compression rheometry, which involves the uniaxial compression of cylinders (Gent, 1960; Hess et al., 2007). We undertook these tests at two scales. At small scale we used a Netzsch GmbH Hyperion® TMA 402 F1 device in which a cylindrical sample 5 mm in diameter and 10 mm in length was set between two ceramic plates and compressed at known applied force (set at 0.1–3 N with 0.2 mN accuracy). The device is encased in a furnace with a maximum temperature of 1775 K and with accuracy (after temperature calibration) of ±2 K. These measurements are performed in air and sample expansion during heating is subtracted as a baseline prior to deformation. The dependent variable is then the change in sample length with time during pressing. At large scale, compression tests were undertaken at high forces using a 300 kN uniaxial press (from Voggenreiter GmbH with an Instron® hydraulic control system upgrade) on cores of Hrafntinnuhryggur obsidian 20 mm in diameter and 40 mm in length. The first iteration (pre-upgrade) of this device and calibration thereof is described in Hess et al. (2007). Linear variable differential transducers (LVDTs) with 10^{-6} m resolution and 150 mm travel range maxima are used with a hydraulic system to operate the position of the upper piston. Force is measured with a Lorenz Messtechnik GmbH K11 load cell with 300 kN working range and an approximate accuracy of 0.05%. While the press can operate in force control mode – wherein the position is the dependent variable of interest – we choose to use it in position control – wherein the force variation with time is the dependent variable of interest. In this position-control mode, the working range of piston velocity is $8.3 \times 10^{-7} \leq u \leq 1.0 \times 10^{-2}$ m.s^{-1} (Wadsworth et al., 2018). A Gero GmbH 3-zone split furnace surrounds the sample and the working pistons either side of the sample with a maximum temperature of 1375 K with a maximum temperature gradient ±5 K on the sample scale in the hot zone. This furnace has a 0.12 m long uniform hot zone when insulated (Cordonnier et al., 2012c). Temperature is recorded

[1] In some published work there is a 2.303 factor in this equation, which is incorporated when the logarithm to the base 10 is used in place of the natural logarithm (Kenderes and Whittington, 2021) which otherwise is not required (Debolt et al., 1976).

[2] We note that in some published sources, what we denote as q_0 is equated to λ_0 (Kenderes and Whittington, 2021), despite the discrepancy in dimensional units between those two parameters.

Table 2
Viscometry data for Krafla rhyolites.

Sample	Measurement type	Temperature (K)*	Viscosity (Pa.s)
IDDP-1	DSC	772	1.72×10^{11}
IDDP-1	DSC	782	8.60×10^{10}
IDDP-1	DSC	805	3.44×10^{10}
Hrafntinnuhryggur	DSC	1004	7.28×10^{10}
Hrafntinnuhryggur	DSC	1007	4.86×10^{10}
Hrafntinnuhryggur	DSC	1026	3.17×10^{10}
Hrafntinnuhryggur	DSC	1031	2.80×10^{10}
Hrafntinnuhryggur	DSC	1034	2.60×10^{10}
Hrafntinnuhryggur	DSC	1034	2.43×10^{10}
Hrafntinnuhryggur	Rotational rheometry	1724	5.13×10^{3}
Hrafntinnuhryggur	Rotational rheometry	1741	4.37×10^{3}
Hrafntinnuhryggur	Rotational rheometry	1758	3.24×10^{3}
Hrafntinnuhryggur	Rotational rheometry	1778	2.24×10^{3}
Hrafntinnuhryggur	Micropenetration	1053	1.58×10^{10}
Hrafntinnuhryggur	Micropenetration	1073	8.13×10^{9}
Hrafntinnuhryggur	Micropenetration	1093	3.47×10^{9}
Hrafntinnuhryggur	Micropenetration	1033	5.75×10^{10}
Hrafntinnuhryggur	Uniaxial compression	993	8.93×10^{10}
Hrafntinnuhryggur	Uniaxial compression	993	7.08×10^{11}
Hrafntinnuhryggur	Uniaxial compression	1013	4.31×10^{11}
Hrafntinnuhryggur	Uniaxial compression	1053	1.93×10^{10}
Hrafntinnuhryggur	Uniaxial compression	1053	4.46×10^{10}
Hrafntinnuhryggur	Uniaxial compression	1038	3.89×10^{10}
Hrafntinnuhryggur	Uniaxial compression	1094	3.55×10^{9}
Hrafntinnuhryggur	Uniaxial compression	1167	3.63×10^{8}
Hrafntinnuhryggur	Uniaxial compression	1238	4.79×10^{7}

* The temperature values have an associated uncertainty of ±1 K.

using K-type thermocouples in the air, sample, and in contact with the pistons. Moreover, in these large-scale experiments, acoustic emissions (AEs), associated with potential cracking events during deformation (Vasseur et al., 2018), are tracked via two piezoelectric AE broadband transducers with 125 kHz frequency. The AE signals are fed to a 40 dB buffered pre-amplifier, and recorded in a Richter data acquisition system at 20 MHz from Applied Seismology Consultants. AE event onsets are triggered and recorded using continuous signals via an autoregressive-Akaike-Information-Criterion (AE-AIC) event picker (Beyreuther et al., 2010). The AE-AIC works by detecting a signal onset by using a short-term average/long-term average (STA-LTA) detector algorithm with a time-window of 1 and 20 ms respectively, with an STA/LTA threshold of 2. The signal is then denoised with an amplitude threshold of 68 dB, before picking the signal arrival time using the minimum of the computed AE-AIC signal (Vasseur et al., 2015).

In both the small- and large-scale compression experiments, we look for one of two responses of the samples to deformation. First, we look for a viscous response, which is found when the force F required to maintain a given axial deformation rate $\dot{\gamma}$ rises and equilibrates at a constant value in the absence of acoustic emissions above background. When this response is observed, we can use a well-known model for the viscosity of the cylindrical sample (Gent, 1960).

$$\mu = \frac{2\pi F h(t)^5}{3V\dot{h}\left(2\pi h(t)^3 + V\right)}, \dot{h} = \frac{\mathrm{d}h}{\mathrm{d}t} \tag{5}$$

where V is the sample volume, $h(t)$ is the time-dependent sample height, F is the force applied at each instant of time, and $\dot{h}$ is the velocity (the first-time derivative of the changing sample height) of the piston, where $\dot{\gamma} = \dot{h}/h_0$ with h_0 the initial height. The second possible response of a sample to deformation is a brittle one, recognized when the force value drops intermittently in sharp punctuated events which can be attributed to sample cracking. AEs are also indicative of brittle responses. Analysis of these deformation modes is discussed extensively elsewhere (Coats et al., 2018; Wadsworth et al., 2018) and applied here. Eq. (5) assumes no slip between the pistons and the sample cylinder contacts, which is visually confirmed post-experiment (i.e., the top and bottom end sample radius is within uncertainty of the initial radius). We apply the Trouton correction where the internal shear strain rate $\dot{\epsilon}$ is $\dot{\epsilon} \approx 3\dot{\gamma}$. All rheological results are given in Table 2.

5. Results and analysis

Our results are divided into (1) the calibration of the shift factor for hydrous rhyolite melts (Section 5a), (2) the determination of the relaxation behavior and associated glass transition temperature intervals for the materials tested herein (Section 5b), (2) a constraint of the temperature-dependence of viscosity (Section 5c), and (3) unrelaxed viscoelastic effects using a universal melt deformation map (Section 5d). Taken together, these results represent characterization of the IDDP-1 and surface rhyolitic magma rheology.

5.1. Calibrating the shift factor for hydrous rhyolite

The shift factor c used in Eq. (1) is important for understanding the relationship between the relaxation temperature window and the viscosity at the glass transition. Gottsmann et al. (2002) showed that c relates to the excess cations $\mathscr{X}$ but did not test the effect of H_2O. Therefore, we present a calibration test using the synthesized sample of Hrafntinnuhryggur composition (remelted) but hydrated to 2 wt% H_2O. Using a cooling and heating rate of $|q| = 10$ K.min^{-1}, we find that the glass transition peak temperature is 764±2 K. Measured using the micropenetration technique (see Section 4), the viscosity at that exact temperature is 8.13×10^{10} Pa.s (with an uncertainty of 0.1 log units). Using Eq. (1), this yields a direct determination of the shift factor by $c = \mu|q| = 1.35 \pm 0.31 \times 10^{10}$ Pa.K.

The above determination of c is within error of the value computed using the anhydrous Hrafntinnuhryggur composition $c \approx 1.21 \pm 0.05 \times 10^{10}$ Pa.K and the anhydrous IDDP-1 composition $c \approx 1.43 \pm 0.14 \times 10^{10}$ Pa.K (see Table 1). The uncertainties on these values of c computed using the Gottsmann et al. (2002) method arise from taking $\pm1\sigma$ standard deviation on the compositions given in Table 1 to compute an upper and lower limit on c. We find that H_2O does not have the same

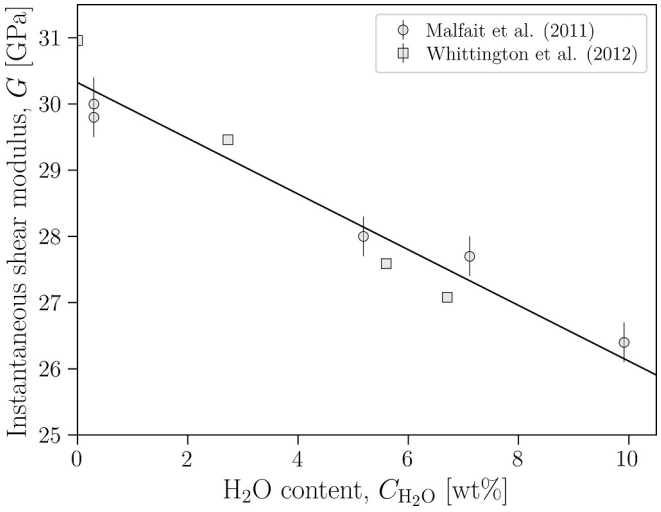

Fig. 4. The dependence of the shear modulus of calc-alkaline metaluminous rhyolite melts on H_2O concentrations; circles (Malfait et al., 2011) and squares (Whittington et al., 2012). The linear regression is $G(C_{H_2O}) = b_1 - b_2 C_{H_2O}$ where $b_1 = 30.23$ GPa and $b_2 = 0.42$ and C_{H_2O} is the water content in wt.%.

effect on the shift factor as the effect of the mol.% excess cations, and we neglect the effect of H_2O on c when c is computed using Gottsmann et al. (2002). To illustrate this further, if we were to compute c using the Gottsmann et al. (2002) model and assuming that the dissolved H_2O is to be incorporated in the mol.% excess cations ($\mathscr{X}$), then for 2 wt% H_2O, we would arrive at $c \approx 8.57 \pm 0.40 \times 10^9$ Pa.K for the Hrafntinnuhryggur base composition (Table 1). This is clearly far lower than the measured value.

The shift factor c relates directly to the shear modulus of the melt G (Schawe and Hess, 2019) such that $c = G\omega$, where ω has units of K^{-1} and is approximately of order unity (Sipp and Richet, 2002). Given that the shear modulus also depends on the dissolved H_2O concentration in rhyolites (Malfait et al., 2011; Whittington et al., 2012), we can account for this possible effect. We compile data for $G(C_{H_2O})$ for rhyolitic melts and demonstrate the weak effect of water on the shear modulus, which can be accounted for by $G(C_{H_2O}) = b_1 - b_2 C_{H_2O}$ where $b_1 = 30.32$ GPa and $b_2 = 0.42$ (**Fig. 4**). If we assume that this $G(C_{H_2O})$ effect contributes to c by the same factor, then using 2 wt% H_2O as the approximate nominal value, then we find that the factor by which c would be modified from a dry composition would be 0.97. Applying this to the dry value of c, we find our dry estimate (i.e., for IDDP-1 using the dry Gottsmann et al., 2002 method) would be reduced to $c \approx 1.39 \pm 0.14 \times 10^{10}$ Pa.K, which is within error of both the measured value, and the original computed value. This means that if there is an effect of H_2O on G that should be propagated to c, then it is either small or it does not exist, and our measurements cannot distinguish these possibilities. Therefore, we do not directly account for H_2O in our determination and use of c. This requires further dedicated investigation to confirm as a general rule for hydrous silicate melts and further work should aim to reduce the uncertainties in the direct determinations of c.

5.2. The glass transition of the IDDP-1 and Hrafntinnuhryggur rhyolitic magma

We find that the IDDP-1 chips have a glass transition onset of 697 ± 3 K and peak of 802 ± 1 K when analyzed as-collected (**Fig. 5a**); that is, on 'first heating' of the glass chips. Similarly, the Hrafntinnuhryggur obsidian has a glass transition onset of 904 ± 5 K and peak of 998 ± 1 K when analyzed as-collected (**Fig. 5a**). When we cool the chips and re-heat them at the same rate, we find that the onset remains around 698 ± 5 K, but the peak is a function of the imposed cooling and heating rate combination (**Fig. 5b**). The measured peak temperatures on cooling-heating cycles are 773 K (at 5 $K.min^{-1}$), 783 K (at 10 $K.min^{-1}$), and 805 K (at 25 $K.min^{-1}$) (**Fig. 5b**). When we apply the same method to the Hrafntinnuhryggur obsidian, we find again that the onset is relatively stable at 923 ± 1.4 K for all heating-cooling cycle rates, but that the peak temperature shifts from 1005 K at 10 $K.min^{-1}$, up to 1035 K at 30 $K.min^{-1}$ (**Fig. 5c**). This relative constancy of the onset temperature as well as the dependence of the peak temperature on the imposed thermal history is well documented and underpins the semi-empirical models that aim to convert these temperatures and rate information into equilibrium viscosities (Wilding et al., 1996; Gottsmann et al., 2002). As expected, the glass transition temperature shifts to higher values for higher rates of matched cooling/heating cycles. Interestingly, following geospeedometry interpretations (Wilding et al., 1996; Lavallée et al., 2015b), the similarity of the first-heating heat flow data (**Fig. 5a**) to the 25 $K.min^{-1}$ matched heating-cooling data (**Fig. 5b**) suggests that the glass chips were quenched during drilling at around 25 $K.min^{-1}$. The natural quench rate of the Hrafntinnuhryggur surface obsidian is slower than 25 $K.min^{-1}$. In **Fig. 5d** we formally apply the geospeedometry methodology (see Eqs. (2–4); Wilding et al., 1996; Lavallée et al., 2015b) to give the computed natural cooling rate for both IDDP-1 and Hrafntinnuhryggur. We find that the cooling rate was likely to be between 7 ± 1 and 80 ± 31 $K.min^{-1}$ for IDDP-1 and around 7 ± 1 $K.min^{-1}$ for Hrafntinnuhryggur.

5.3. Relaxed melt viscosity

The rheological measurements undertaken at low loads – that is all results obtained from the micro-penetration measurements, the thermo-mechanical analysis, and the uniaxial press under low strain rates – provide a constant 'relaxed' value of viscosity and a single value of viscosity for a given temperature, irrespective of the applied conditions. No vesiculation occurred during these tests. Thus, we deem the viscosity obtained to represent the viscosity of a Newtonian system at these conditions. Moreover, the results from the thermal analysis (**Fig. 5**) can be used to estimate the relaxed melt viscosity at the glass transition temperature Section 4b). In order to understand these viscosity values, together with the viscosity values from our rheological study (Section 4a), we use the empirical non-Arrhenian Vogel-Fulcher-Tammann (VFT) viscosity law in functional form

$$\mu(T) = \mu_0 \exp\left(\frac{B}{T - T_0}\right) \tag{6}$$

where μ_0, B, and T_0 are constants to be determined. As discussed (Section 1) the primary difference between the IDDP-1 rhyolite and the surface Hrafntinnuhryggur rhyolite is the dissolved H_2O concentration in the melt, which in turn has a first-order control on the viscosity (Hess and Dingwell, 1996; Giordano et al., 2008). Hess and Dingwell (1996) used a parameterization via $\mu_0 = a_1 + a_2 \ln(C_{H_2O})$, $B = a_3 + a_4 \ln(C_{H_2O})$, and $T_0 = a_5 + a_6 \ln(C_{H_2O})$ for which $a_1 = -8.163$, $a_2 = 1.918$, $a_3 = 22107$, $a_4 = 5453$, $a_5 = 195.7$ and $a_6 = 32.25$. These constants are found by performing a global minimization of Eq. (3) to experimental test data from published sources (Friedman et al., 1963; Shaw, 1963; Burnham, 1964; Persikov et al., 1990; Hess et al., 1995; Baker, 1996; Dingwell et al., 1996; Schulze et al., 1996; Dorfman et al., 1996; Scaillet et al., 1996) that were collected using similar techniques to those employed herein. Here, we compile those same data in order to visually assess the quality of the minimized model (Figs. 6a & 6c). We find that the fit is reliable at predicting the data with particular efficacy at $C_{H_2O} \leq 4$ wt% (Fig. 6a) which encompasses the values found for IDDP-1 and other Krafla rhyolites (Tuffen and Castro, 2009; Zierenberg et al., 2013; Watson, 2018; Saubin et al., 2021).

Using our data for Hrafntinnuhryggur and for IDDP-1, we can fit the Hess and Dingwell (1996) viscosity model for the best-fit H_2O

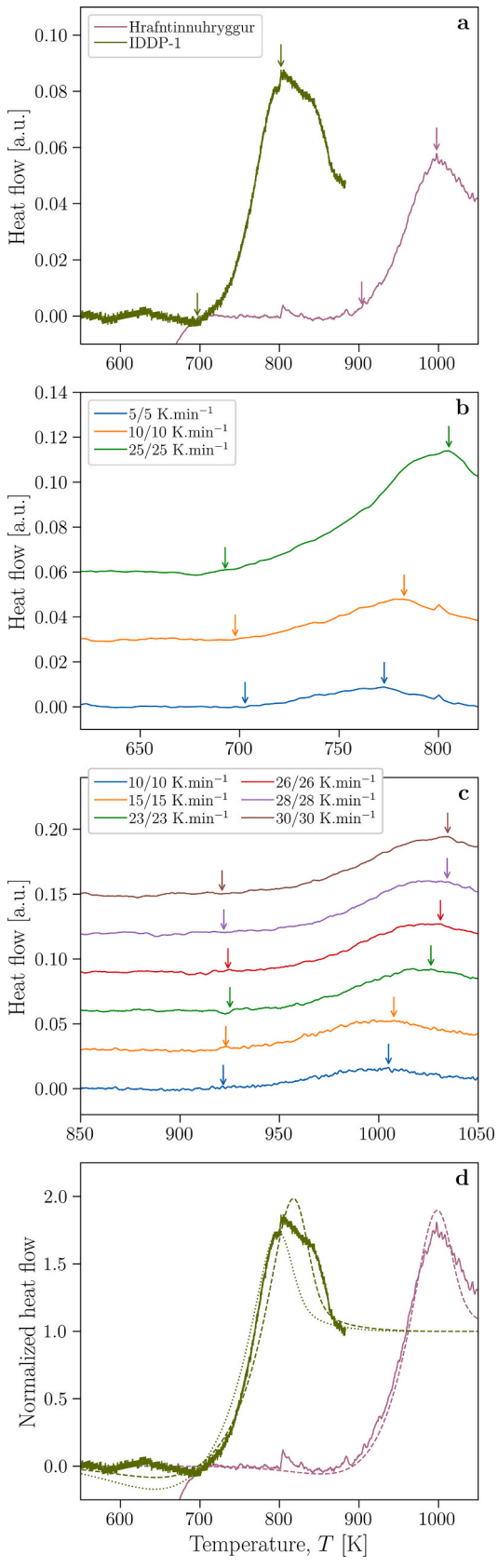

(caption on next column)

Fig. 5. Structural relaxation of IDDP-1 and Hrafntinnuhryggur glass chips cast as heat flow (arbitrary units) as a function of temperature as chips are heated at a constant rate. All datasets are baseline-subtracted. (a) The heat flow of an IDDP-1 and a Hrafntinnuhryggur glass chip on first heating (heated at 25 K.min^{-1}). For the IDDP-1 signal, we note there is a 'notch' on the peak of the glass transition where the arrow is indicating (see panel d). (b) The same IDDP-1 glass chip as used for (a) but here cooled and then reheated at matching rates from 5 K.min^{-1} to 25 K.min^{-1}. In all cases, the onset and peak of the glass transition hump are marked with arrows, found by using a peak-finding algorithm (for the peak) and the intersection of two linear regressions through the curve (for the onset). (c) Heat flow of the same surficial obsidian glass chip from Hrafntinnuhryggur as used for (a) at different cooling/heating rate cycles. (d) The same curves as in (a) but here normalized as $(\beta - \beta_g)/(\beta_l - \beta_g)$; see Section 4 for details. The dashed curve fits are the best-fit geospeedometry models (see Section 4b) for cooling rates of 7 K.min^{-1}, for IDDP-1 and Hrafntinnuhryggur. The dotted curve on the IDDP-1 signal is the same model but for 80 K.min^{-1} which, by eye, matches the rising signal on the low temperature side of the glass transition peak and appears to better reproduce the 'notch' in the peak. This leads us to conclude that 7 – 80 K.min^{-1} with $\mathscr{O}(50)$ K.min^{-1} are reasonable constraints.

concentration. To do this, we use a least-squares minimization (Kemmer and Keller, 2010). However, in order to capture the uncertainty associated with the shift factor c (see Section 5a), which impacts the viscosity values derived from DSC measurements, we take a Monte Carlo approach. First, we assume that the real value of c is given by a normal probability distribution with the best estimate c as the mean, and the uncertainty on c as the standard deviation about the mean. Then we draw a value of c from this distribution and use it to locate the DSC data in a viscosity plot (Fig. 6). Finally, we fit for H_2O using Hess and Dingwell (1996) via Eq. (3). We then repeat this 10^6 times, thereby capturing the effect of the uncertainty on c.With the results, we then take the mean and standard deviation of the H_2O concentrations so that the quoted global best-fit value is C_{H_2O} and the uncertainty is given by the standard deviation of the best-fit values of H_2O. In the case of IDDP-1, this results in a global fit of $C_{H_2O} = 2.12 \pm 0.08$ wt%. In the case of Hrafntinnuhryggur, this results in $C_{H_2O} = 0.12 \pm 0.01$ wt% (we note that ± 0.01 wt% is the uncertainty on the fit across all data, which is larger than the uncertainty associated with randomly varying c as described above). Other viscosity models could have been used to perform this minimization (Romine and Whittington, 2015).

5.4. Unrelaxed behavior and melt rupture

Here we explore the results of the high-load compression tests in which large 20 mm diameter samples of the Hrafntinnuhryggur obsidian were deformed under high relative rates of axial strain. The experiments, which had either a measured force drop, a measured acoustic emission signal, or both, were denoted as brittle, whereas the rest were denoted as viscous. New results presented here are combined with published results using the same obsidian (Tuffen et al., 2008; Wadsworth et al., 2018) and other melts (Dingwell and Webb, 1989) in order to explore a universal threshold for unrelaxed melt rupture (brittle) in response to stress.

To analyze our results, we use the framework given by Wadsworth et al. (2018). First, we constrain the melt relaxation timescale $\lambda = \mu/G$ and the deformation timescale $\lambda_d = \dot{\epsilon}^{-1}$, which can be combined in a dimensionless Weissenberg number $\mathrm{Wi} = \lambda/\lambda_d = \mu\dot{\epsilon}/G$. Here, $\mathrm{Wi} \ll 1$ is the case where the relaxation time is relatively short compared with the deformation time, such that there is sufficient time for relaxation of the melt during flow and bulk relaxed viscous behavior is expected. By contrast, $\mathrm{Wi} \gg 1$ is the case where the deformation time is short and unrelaxed behavior can be expected. Because significant strain is reached in our tests, the high-Wi regime can result in substantial accumulation of stress and bulk brittle responses. As Wi exceeds a critical value, this can result in solid-like behavior and wholesale melt rupture

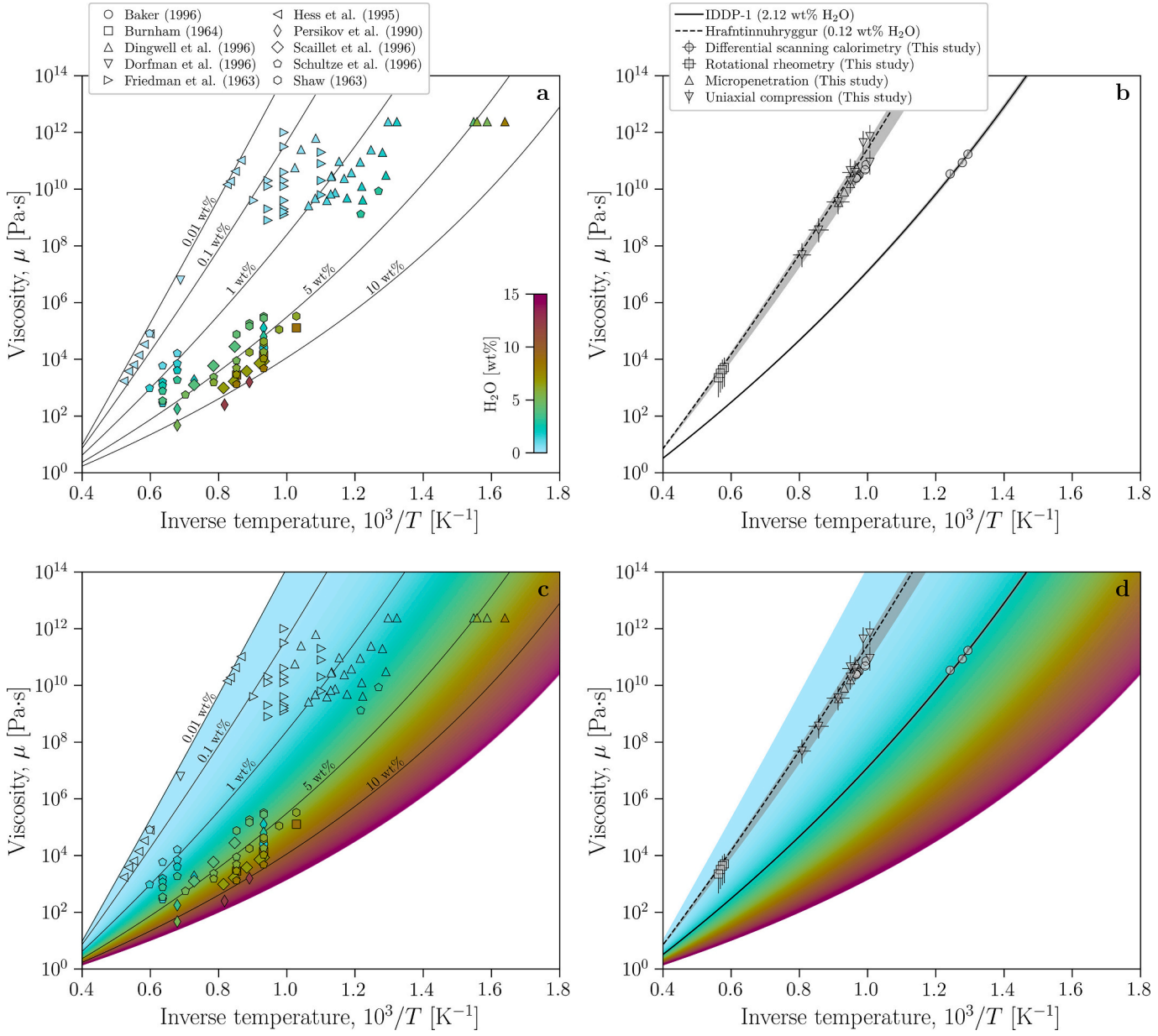

Fig. 6. The viscosity of the model rhyolite 'haplogranite' system (color-coded) compared with the measured viscosity of the Hrafntinnuhryggur rhyolite and IDDP-1 glass chips. (a) The model haplogranite system with data from direct viscometry measurements compiled from published sources (Friedman et al., 1963; Shaw, 1963; Burnham, 1964; Persikov et al., 1990; Hess et al., 1995; Baker, 1996; Dingwell et al., 1996; Schulze et al., 1996; Dorfman et al., 1996; Scaillet et al., 1996) all used to underpin a widely-used rhyolite viscosity model (Hess and Dingwell, 1996). Indicative solid curves at chosen water contents 0.01, 0.1, 1, 5, and 10 wt.% are given to help guide the reader. The data symbols are also color-coded in accordance with their measured water content. (b) The same H_2O-dependent rhyolite model as given in (a) but here compared with data from Hrafntinnuhryggur (Wadsworth et al., 2022a) and the differential scanning calorimetric constraints provided for IDDP-1 herein (see text). The dashed curve is the Hess and Dingwell (1996) model for 0.12 wt.% H_2O and the solid black curve is the same model for 2.12 wt.% H_2O. The grey band either side of the Hrafntinnuhryggur data represents the range of H_2O concentrations measured for Hrafntinnuhryggur (upper bound 0.2 wt.%; lower bound 0.1 wt.%;Tuffen and Castro, 2009); this band is wider than the uncertainty on the fit for H_2O (±0.01 wt.%). The grey band either side of the IDDP-1 data represents the Monte Carlo uncertainty (see text) on the best-fit H_2O (±0.08 wt.%). Panels (c) and (d) are the same as panels (a) and (b), respectively, but with the Hess and Dingwell (1996) model contoured in a continuous color map.

(Cordonnier et al., 2012c; Coats et al., 2018; Wadsworth et al., 2018). We note that in Coats et al. (2018), Wi is given as a Deborah number De, which should be reserved for oscillatory deformation and is only equivalent to Wi when the Cox-Merz rule is assumed correct. The same brittle regime can be inferred from other work (e.g., via textural analysis and acoustic emission monitoring) even if Wi is not explicitly constrained (Lavallée et al., 2008, 2013; Kendrick et al., 2013). Wadsworth et al. (2018) found that across a wide range of sample compositions, including the Hrafntinnuhryggur obsidian, Wi = 0.04 is the critical value above which melt will rupture, and that the window $0.01 \leq \mathrm{Wi} \leq 0.04$ is the transition from viscous to brittle behavior for increasing Wi.

Our data for the deformation of Hrafntinnuhryggur glass matches the prediction that $\mathrm{Wi} \geq 0.04$ will result in a brittle response (**Fig. 7**) and push the validation of this viscoelastic theory to lower values of λ (i.e., higher temperatures) and lower values of λ_d (i.e., higher deformation rates) than tested previously.

For comparison we add data from Wadsworth et al. (2024) in which crystal-rich lavas with crystallinities up to 0.55 and low porosity (<0.01)

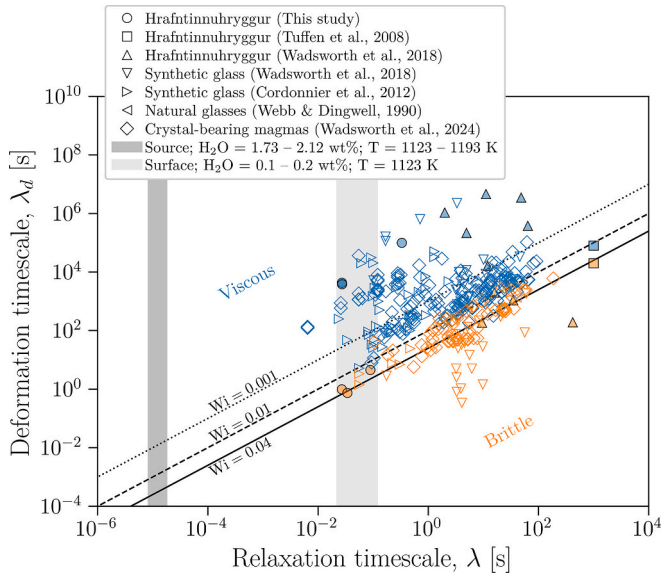

Fig. 7. The viscoelastic rheology of rhyolite glass at Krafla, Iceland. We measure the response of samples to deformation at a constant rate of axial strain $\dot{\gamma}$: the response is viscous (blue points) if the evolution of the measured stress evolves smoothly toward an equilibrium value and is brittle (orange points) if there are drops in the stress that are associated with acoustic emissions or audible cracking. Here we compile existing data for synthetic glasses (Cordonnier et al., 2012c; Wadsworth et al., 2018), crystal-bearing glass (Pistone et al., 2012; Cordonnier et al., 2012b), natural glass compositions (Webb and Dingwell, 1990), natural dome lavas (Lavallée et al., 2007, 2013; Kendrick et al., 2013; Coats et al., 2018), and Hrafntinnuhryggur lavas (Tuffen et al., 2008; Wadsworth et al., 2018). The black curves represent a constant ratio (termed a Weissenberg number Wi) between the deformation timescale and the relaxation timescale of Wi = 0.04 (dotted line), Wi = 0.01 (dash line), and Wi = 0.001 (solid line) (see text). The vertical zones represent the estimated conditions of λ for lava emplacement (labelled 'surface') and IDDP-1 (labelled 'source' and informed by our rheology estimates; Figs 4 & 5).

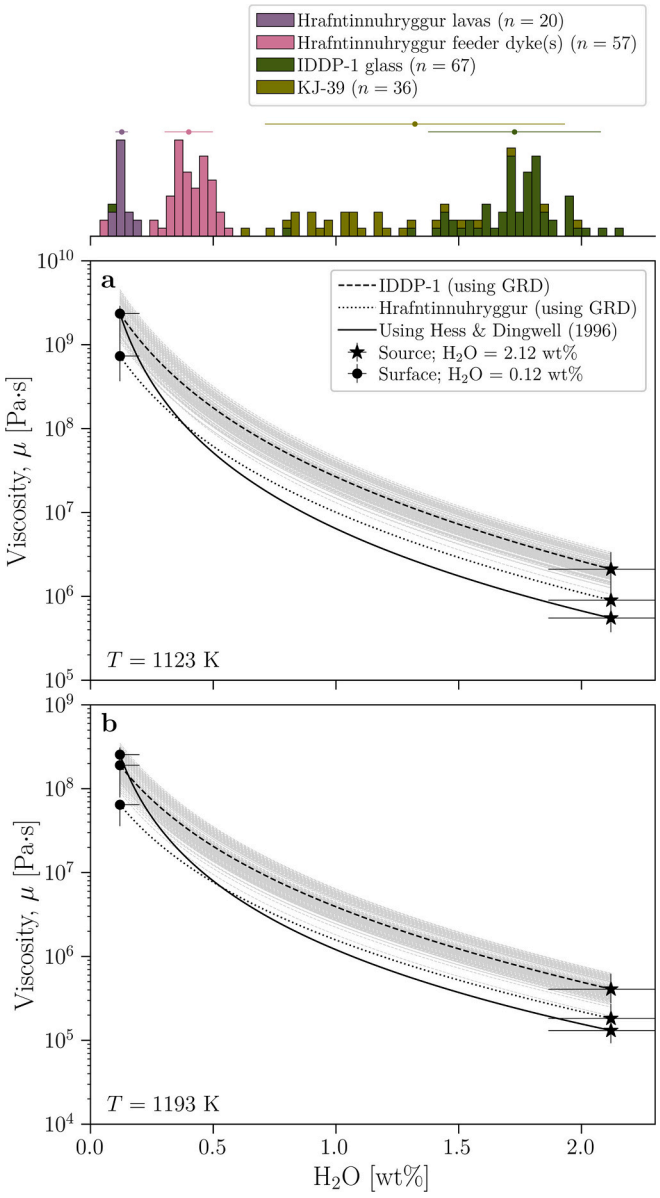

Fig. 8. The relationship between the computed viscosity μ and the H_2O concentration in the glass (C_{H_2O}) showing the estimated source values (stars; derived from calorimetry) and the measured surface values (points) assuming the estimated storage temperature of (a) $T = 1123$ K and (b) $T = 1193$ K (Zierenberg et al., 2013; Masotta et al., 2018). The solid black curve is plotted using the Hess and Dingwell (1996) model (see **Fig. 4**), the dotted and dashed black curves are plotted using the Giordano et al. (2008) model and an average of the Hrafntinnuhryggur and IDDP-1 glass compositions, respectively (see **Fig. 1**). The grey curves are plotted using the Giordano et al. (2008) model with all individual glass analyses from IDDP-1. Above the plot is a histogram of measured C_{H_2O} values from: (1) Hrafntinnuhryggur lavas $n = 20$ (Tuffen and Castro, 2009; Ryan et al., 2015a; Wadsworth et al., 2019; Seropian et al., 2022); (2) Hrafntinnuhryggur feeder dyke(s) approximately 35–50 and 90 m below the paleo-surface $n = 57$ (Tuffen and Castro, 2009; Tuffen et al., 2010; Foster et al., 2024); and (3) KJ-39 $n = 36$ (Rule, 2020) and IDDP-1 glass chips $n = 67$ (Zierenberg et al., 2013; Lowenstern and Pitcher, 2013; Watson, 2018; Bindeman et al., 2021; Saubin et al., 2021).

were deformed in the same way. To analyze those samples, Wadsworth et al. (2024) adapt both the relaxation and the deformation timescales to accommodate the presence of crystals and pores. This framework is then compared with previous data for the deformation of natural, porous, crystal-bearing lavas (Lavallée et al., 2007, 2013; Kendrick et al., 2013; Coats et al., 2018), crystal-bearing synthetic glasses (Cordonnier et al., 2012a) and crystal-bearing synthetic glasses with nominally low porosity (Pistone et al., 2012). Here, all of these results are given as 'Wadsworth et al. (2024)' on the grounds that the re-calculation of the relaxation and deformation timescales (that locates them in Fig. 7) originates therein. Because these results provide a dimensionless framework for predicting the viscous-to-brittle transition in flowing rhyolites of variable crystallinity, they therefore also show that this deformation map (**Fig. 7**) should be valid for the crystal-bearing components of the sub-surface at Krafla, such as partially molten felsite, or Krafla rhyolite glass that undergoes rapid crystallization (Cáceres et al., 2021).

5.5. Additional H_2O concentration data for the Hrafntinnuhryggur feeder dyke

The H_2O determinations found here for the feeder dyke system are 0.25–0.55 wt% (see Supplementary Data). These supplement existing data from FTIR for the same feeder dyke rocks (Tuffen and Castro, 2009; Foster et al., 2024), data for the surficial lavas (Tuffen and Castro, 2009), data for KJ-39 retrieved glass (Rule, 2020), and data for chips recovered from IDDP-1 (Zierenberg et al., 2013; Lowenstern and Pitcher, 2013; Watson, 2018; Bindeman et al., 2021; Saubin et al., 2021). In **Fig. 8** we show a histogram of these H_2O data which reveal the full spectrum of water concentration between the degassing conditions at the surface (at Hrafntinnuhryggur) and the average ~1.73 wt% quenched in during IDDP-1 drilling. Interestingly, the glass chips retrieved from drilling

mud show quenched magma can ultimately hold a wide range of H_2O concentrations presumably as variable extents of degassing may take place due to drilling activities prior to quenching. Importantly, the continuum in water concentration in **Fig. 8** indicates that a spectrum of melt viscosity co-exists in the system perturbed by drilling activity.

6. Discussion

Our results constrain the viscosity and viscoelastic rheology (up to and including the brittle limit) of rhyolites at Krafla volcano including the first-order effects of temperature and H_2O concentration. We have exploited the fact that at Krafla, quenched samples of pristine rhyolitic magma are available from both the shallow storage reservoir and the surface, in order to examine how the rheology changes up through the shallow crust. Here, we explore these results in the context of the goals of the Krafla Magma Testbed (KMT) and outline how these results can be used in future work to prepare for new drilling campaigns at Krafla. The aim of the KMT is to pursue further drilling opportunities at Krafla volcano in order to cross a 'last unexplored frontier' (see https://www.kmt.is/) and monitor and explore our magma filled crust. Ultimately, endeavors such as these are potentially hazardous simply because the response of rhyolite to drilling is poorly understood. Magmas are increasingly considered as desirable environments to augment geothermal energy supply but ultimately, endeavors such as these require a robust quantification of magma rheology.

6.1. The viscosity and rheology of rhyolites from storage to the surface

Our results relate the H_2O concentrations to the viscosity via the model of Hess and Dingwell (1996) (Fig. 6). If we now take the bounds on the predicted IDDP-1 storage temperature of 1123–1193 K (Zierenberg et al., 2013) we can demonstrate how our validated model for the viscosity varies with H_2O concentration (**Fig. 8**). The lower bound on the viscosity at this temperature is the storage viscosity $\sim 1.31 - 5.50 \times 10^5$ Pa.s (constrained with the relaxation of IDDP-1 glass chips; Fig. 6b), whereas the upper bound on the viscosity at this temperature is the surface viscosity $\sim 2.35 \times 10^9$ Pa.s (constrained via relaxation and rheometry using the Hrafntinnuhryggur glass; Fig. 6b). We can acknowledge that the eruption temperature of the Krafla rhyolites, leading to the emplacement of Hrafntinnuhryggur, may be lower than the storage temperature of 1123–1193 K, such that the surface viscosity given in **Fig. 8** could be higher. For example, if we take the lower relative storage temperature estimate for the Chaitén 2008 rhyolite of 1098 K (Castro and Dingwell, 2009), then the viscosity would be $\sim 5.62 \times 10^9$ Pa.s. Nevertheless, the model constraints provided herein allow this to be computed if the eruption temperature is known.

Here, we focus on the Hess and Dingwell (1996) model for viscosity, which is specifically calibrated for rhyolites. If instead we use a composition-dependent model (Giordano et al., 2008), we see that the differences associated with the small compositional variations between IDDP-1 and Hrafntinnuhryggur glasses are minor compared with the effect of dissolved H_2O (**Fig. 8**).

Our results imply that future magma drilling efforts at Krafla as part of KMT must constrain the evolution of dissolved H_2O, due to perturbations in pressure and temperature associated with drilling, in order to predict the evolution of viscosity accurately. Given that these rhyolites have a propensity to fracture when cooled and pushed to strain at an increased rate (**Fig. 7**), these parameters will be of importance to predict if and/or when brittle failure and fragmentation may occur in response to drilling.

The deformation map presented in Fig. 7 can be used to understand the conditions of strain rate required for failure to occur. However, the deformation map presupposes that the strains will be large (Wadsworth et al., 2018). In fact, it takes a finite time – and therefore strain – for the failure to onset and this time is not accounted for by the deformation map scaling given here. Instead, to find the time for failure we use Maxwell's viscoelasticity which states

$$\sigma + \frac{\mu}{G}\frac{d\sigma}{dt} = \mu\dot{\epsilon} \tag{7}$$

where σ is the shear stress in the melt. If $\dot{\epsilon}$ and μ are both constant, as is the case in our experiments, and if $\sigma = 0$ at $t = 0$, then Eq. (7) leads to a prediction of $\sigma(t)$ (as)

$$\sigma(t) = \mu\dot{\epsilon}\left[1 - \exp\left(-\frac{tG}{\mu}\right)\right]. \tag{8}$$

Our experimental finding that failure occurs for $Wi \geq 0.04$ is akin to finding that the critical stress for failure is $\sigma_c = 0.04G \approx 4 \times 10^8$ Pa. Eq. (8) can then be used to find the critical time t_c it takes for σ to reach σ_c (as)

$$t_c = -\frac{\mu}{G}\ln\left(1 - \frac{\sigma_c}{\mu\dot{\epsilon}}\right) \tag{9}$$

or, as a finite strain required for failure ϵ_c

$$\epsilon_c = -\mathrm{Wi}\ln\left(1 - \frac{\sigma_c}{\mu\dot{\epsilon}}\right) \tag{10}$$

Eqs. (9 and 10) then acknowledge that there can be viscous deformation occurring for a finite time (or strain) prior to viscoelastic rupture, which has been confirmed experimentally (Dingwell and Webb, 1989; Cordonnier et al., 2012c; Wadsworth et al., 2018; Namiki et al., 2023). Note that Eqs. (8–10) are specific to the case where strain rate is held constant and in cases of variable strain rate, a numerical solution to Eq. (7) is required.

6.2. Potential rheological impact of microlites, nanolites, and iron oxidation

The viscosity of silicate magma is influenced by both melt chemistry and the presence of crystals. In the case of Krafla, the rhyolitic magma contains a high concentration of iron. In **Fig. 9** we report the average glass total iron (FeO_T) as a function of the silica (SiO_2) as compared with rhyolite glasses worldwide using a published database (Di Genova et al., 2017). This shows that the Hrafntinnuhryggur obsidian and IDDP-1 glass are among the most iron-rich natural rhyolitic glasses known (Wadsworth et al., 2021a).

Iron can play a role in magma rheology due to changes in oxidation state, which impacts the configuration and role of iron in the melt structure (Dingwell, 1991). Additionally, iron can promote crystallization, including the formation of iron-rich nanolites (Mujin et al., 2017; Di Genova et al., 2018; Di Genova et al., 2020; Cáceres et al., 2020, 2021, 2024; Okumura et al., 2022; Pereira et al., 2024). Interestingly, the precipitation of iron-rich nanolites can have a knock-on effect on the melt viscosity which can, in some cases, be substantial (Zandonà et al., 2023; Cáceres et al., 2024; Pereira et al., 2024). Having said that, the volume fractions of nanolites tend to be small (Okumura et al., 2022), reducing their expected effect on the bulk magma viscosity (Mader et al., 2013; Vasseur et al., 2023) and the direct compositional effects involving the role of iron tends to be small relative to the effects of temperature and water (Chevrel et al., 2014).

The formation and growth of Fe-oxide crystals in Krafla rhyolite can result from oxidation of the melt (Cáceres et al., 2021). Contrastingly, Castro et al. (2009) showed that the formation of Fe-oxide crystals can reduce the melt in an oxidation state buffered crystallization step associated with H_2O movement. Casas et al. (2019) used titration methods to determine the iron oxidation ratio in the Hrafntinnuhryggur as-collected glass, and found that the ratio of Fe^{3+} to total Fe, termed Fe_T, was $Fe^{3+}/Fe_T = 0.167$, similar to the 'clear glass' in the spherulite-bearing samples ($Fe^{3+}/Fe_T = 0.165 \pm 0.04$) reported by Castro et al. (2009). Other than these sparse measurements, the oxygen fugacity for each

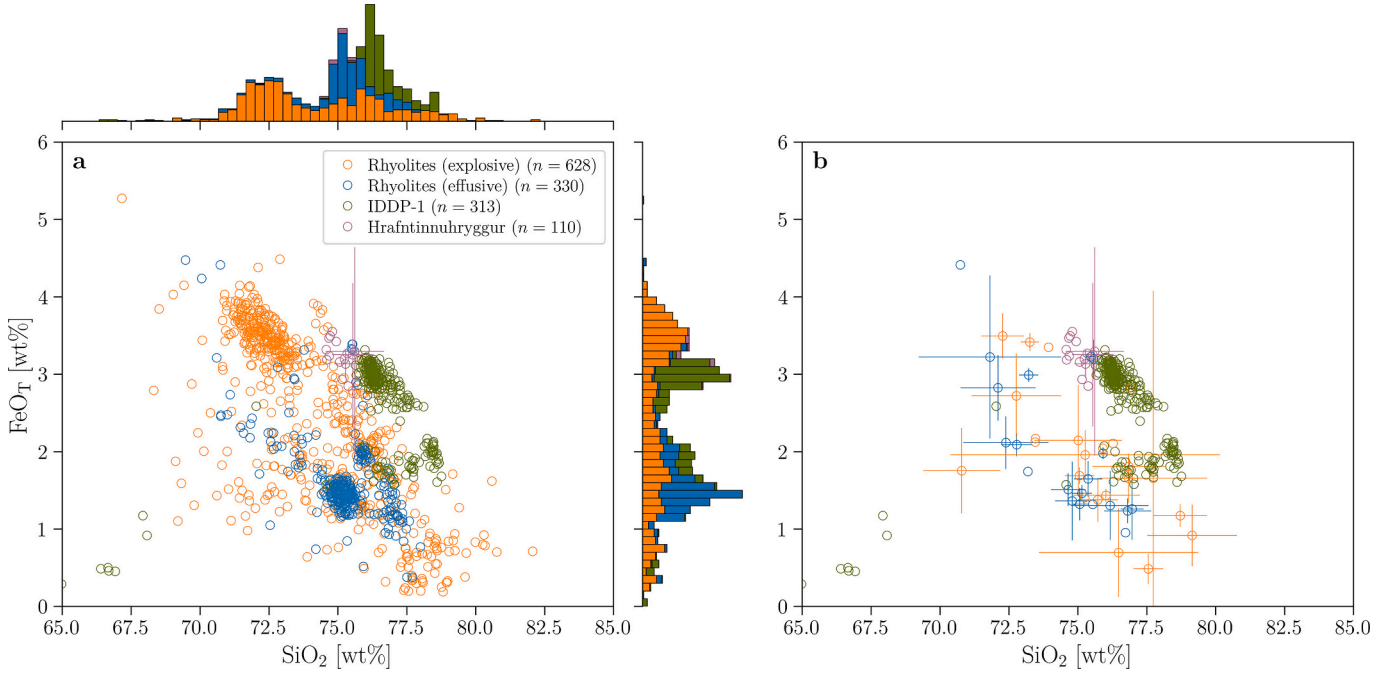

Fig. 9. The major element composition of the Hrafntinnuhryggur rhyolite glass (purple) and the IDDP-1 glass (green) using the published major element analysis with associated uncertainty (Tuffen and Castro, 2009; Zierenberg et al., 2013; Masotta et al., 2018; Saubin et al., 2021). Here, we compare those compositions with rhyolite glass measurements split into the products of explosive eruptions and the products of effusive eruptions worldwide (Di Genova et al., 2017). The Hrafntinnuhryggur and IDDP-1 rhyolites are especially iron-rich when compared with a global distribution of effusive lavas (see the histogram associated with the C_{FeO_T} data here) with implications for the propensity for nanolite formation. Compositions are re-normalized to anhydrous 100%. (a) All individual analyses. (b) Only the mean of any given eruption product. Note that (b) is more representative because it acknowledges that most of the high-FeO$_T$ analyses in (a) come from a single eruption (Cordón Caulle 2011-12; Chile).

rhyolite body at Krafla is poorly constrained and so this effect of iron on melt structure and rheology should be investigated further in future.

Our deformation map (**Fig. 7**) suggests that this growth of any crystals will strongly affect the viscoelastic properties if the crystallization reaches high volume fractions relative to a 'maximum packing' fraction (Wadsworth et al., 2024). For example, if crystallinities were to reach $\approx$ 40 vol.%, then the viscosity would increase by one log unit (Mader et al., 2013). Clearly, iron-bearing nanolites cannot crystallize to such high volume fraction. However, if the rhyolite is stored hot for sufficient time for further crystallization, or if another rhyolite which has crystallized is intersected by drilling at Krafla, then our deformation map can be used to constrain the rheology (Fig. 7).

Future work should explore whether interactions with drilling fluids and/or drilling-induced decompression and cooling could trigger sufficient oxidation of iron to induce nanolite or microlite formation (Di Genova et al., 2018; Cáceres et al., 2021) before quenching. Importantly, the fact that the clear-glass IDDP-1 glass chips (Saubin et al., 2021), such as the chips used here, conform to the Hess and Dingwell (1996) viscosity model appears to demonstrate that nanolites did not form, based on the assumption that their presence would influence the rheology measured. However, the so-called brown glass explored by Saubin et al. (2021) and others may contain nanolites.

6.3. *The transport system from the source to surface and implications for KMT and drilling*

We have direct access to rhyolite at the storage region (via IDDP-1) and the surface (via Hrafntinnuhryggur) or the near-surface (via the Hrafntinnuhryggur feeder dyke system). The surface Hrafntinnuhryggur rhyolites appear texturally indistinguishable from effusive lavas (cf Fink, 1983). However, Foster et al. (2024) found evidence that these lavas are formed from welding of ash-sized particles, similar to the processes that form welded and rheomorphic ignimbrites (cf Branney and Kokelaar, 1992), supporting the so-called 'cryptic fragmentation' rhyolite emplacement model (Wadsworth et al., 2020; Wadsworth et al., 2022b) as a basis for rhyolite dyke and lava emplacement. Weaver et al. (2023) additionally showed that secondary vesiculation and sintering occurs in breccia zones. In this model, magma fragmentation is vigorous and occurs at depth, producing pyroclasts that are transported up the conduit where a fraction of the pyroclasts are 'captured' at shallow depths and weld to the conduit walls. Those welded deposits are then advected out of the vent as lava. This is pertinent to the drilling scenarios because it suggests that the Krafla rhyolites can readily fragment in vigorous explosive eruptions when subjected to a decompression (Rooyakkers et al., 2020).

The observation during the IDDP-1 drilling was that no catastrophic fragmentation occurred. That is, drilling intercepting magma did not produce an eruption (Ilic et al., 2020). Nevertheless, understanding the range of behaviors that are possible with this rhyolite or any other rhyolite is critical to understanding the generalized suite of possible responses magma could exhibit during drilling.

Traditional conceptual models (those that do not invoke vigorous fragmentation) for silicic lava formation invoke buoyant magma rise with outgassing during ascent (Eichelberger et al., 1986) Jaupart and Allègre, 1991; Westrich and Eichelberger, 1994; Cassidy et al., 2018). If this is the case, then it is clear how the H_2O concentrations – and associated viscosities at magmatic temperatures – measured here, evolve through the crust. In these models, H_2O is lost through diffusion into nucleating and growing bubbles, and/or into opening fractures (Eichelberger et al., 1986; Gonnermann and Manga, 2003; Castro et al., 2012). Fracturing, shown to have been occurring in the shallow feeder system at Hrafntinnuhryggur during lava emplacement in the brittle field (cf. **Fig. 7**; Wadsworth et al., 2018), would serve to further enhance gas escape (Yoshimura and Nakamura, 2008; Sano et al., 2015; Lamur et al., 2017). So the vesiculating, frothing, and fracturing rise of rhyolite during drilling is another scenario that should be explored.

In the Wadsworth et al. (2020) model, the majority of H_2O loss from storage to the surface is likely to occur into rapidly growing bubbles prior to and during explosive fragmentation. Upon fragmentation, this H_2O is then liberated into the conduit gas, which separates from the magma and accelerates up and out of the system. Wadsworth et al. (2020) predict that at the fragmentation level (a minimum of 1 km depth), the melt H_2O concentration has already dropped to ~0.5 wt%. Above this fragmentation point, continued degassing to very low H_2O concentrations is driven by time-dependent diffusive outgassing out of bubbly particles that were formed at fragmentation and which are transported through a relatively low-pressure dusty gas (Wadsworth et al., 2020; Wadsworth et al., 2022b; Weaver et al., 2022). Importantly, this degassing impacts the timescale of sintering (welding) which ultimately shuts the permeable pathways and controls the final concentration of dissolved volatiles in shallow systems (Wadsworth et al., 2021b; Weaver et al., 2023).

We highlight here these different models for rhyolite ascent in the crust on the assumption that future drilling into magma has some conceptual similarities to opening up a conduit to the Earth's surface. For this reason, the general behavior of rhyolite upon decompression and ascent to the surface requires understanding. Our thermal analysis indicates that the IDDP-1 magma underwent the glass transition (T_g) at ~793 K, and was likely quenched at a rate of 7–80 K.min^{-1} (see **Fig. 5**). Considering storage temperatures of ca. 1123–1193 K, the interval between storage temperature and T_g, and the cooling rate through T_g, we have constrained both a thermal window (of ~400 K), and a very abbreviated timescale (~4–60 min) during which magma responds physically and chemically to pressure-temperature perturbations imparted by drilling activity.

7. Closing remarks

We used thermal analysis and several rheological apparatuses to measure the glass transition interval, the cooling rate, the viscosity and the viscoelastic rheological (brittle) limit of Krafla obsidian glass sampled from surficial lava, a shallow dyke, and the drilling mud from IDDP-1. We find that the IDDP-1 glass chips underwent the glass transition at ~793 K, by being quenched at a rate of 7–80 K.min^{-1}, constraining a temperature-time window for physico-chemical perturbation by drilling activity. Rheologically, we use the Hess and Dingwell (1996) model for rhyolites to reproduce the viscosity of the variably hydrous (shallow and deep) rhyolitic magma and demonstrate the weak effect of water on the shear modulus of rhyolitic melts. Our analysis surmises the importance of iron, whose concentration is elevated in Krafla rhyolite, on the potential rheological response of magma to transport or drilling. Finally, our rheological analysis indicates that deformation of aphyric Krafla magma at Wi $\geq$ 0.04 will favor a brittle response, and that if partially crystallized (e.g., the felsite capping the magma body) the deformation map provided herein should be valid to model the conditions for viscous flow and fragmentation. We conclude that these rheological constraints on the Krafla rhyolitic magmas at storage and surface conditions should be used in conjunction with simulations of magmatic processes in response to drilling scenarios to provide a scientific basis for hazard assessment and risk mitigation for the KMT project.

CRediT authorship contribution statement

Fabian B. Wadsworth: Writing – original draft, Visualization, Funding acquisition, Formal analysis, Conceptualization. **Jérémie Vasseur:** Writing – review & editing, Visualization, Formal analysis. **Yan Lavallée:** Writing – review & editing, Conceptualization. **Kai-Uwe Hess:** Writing – review & editing, Formal analysis, Conceptualization. **Jackie E. Kendrick:** Writing – review & editing, Resources, Funding acquisition. **Jonathan M. Castro:** Writing – review & editing, Resources. **Daniel Weidendorfer:** Writing – review & editing, Resources, Formal analysis. **Shane M. Rooyakkers:** Writing – review & editing, Resources. **Annabelle Foster:** Writing – review & editing, Visualization. **Lucy E. Jackson:** Writing – review & editing. **Ben M. Kennedy:** Writing – review & editing, Resources. **Alexander R.L. Nichols:** Writing – review & editing. **C. Ian Schipper:** Resources. **Bettina Scheu:** Writing – review & editing, Funding acquisition. **Donald B. Dingwell:** Writing – review & editing, Funding acquisition. **Tamiko Watson:** Resources, Formal analysis. **Georgina Rule:** Resources, Formal analysis. **Taylor Witcher:** Writing – review & editing, Formal analysis. **Hugh Tuffen:** Writing – review & editing.

Declaration of competing interest

The authors declare that they have no known competing financial interests or personal relationships that could have appeared to influence the work reported in this paper.

Data availability

All data is provided with the manuscript.

Acknowledgments

We are grateful to the wider Krafla Magma Testbed team for their support and to Landsvirkjun in particular. Thanks to Julia Schunke, Francisco Caceres, Holly Unwin, Ed Llewellin, and Marize Muniz da Silva for general discussion or field assistance. Funding was provided by the European Research Council (834225-EAVESDROP; 101001065-MODERATE) and by the Natural Environment Research Council of UKRI (grant number NE/T007796/1). Yan Lavallée, Jackie Kendrick, and Donald Dingwell acknowledge support from LMUexcellent, funded by the Federal Ministry of Education and Research (BMBF) and the Free State of Bavaria under the Excellence Strategy of the Federal Government and the Länder. BS acknowledges funding from the European Union's Horizon 2020 research and innovation programme under grant agreement No 858092 (MSCA-ETN IMPROVE). We thank the landowners at Hrafntinnuhryggur. Two reviewers and the editor Shane Cronin all helped to improve the manuscript.

Appendix A. Supplementary data

Supplementary data to this article can be found online at https://doi.org/10.1016/j.jvolgeores.2024.108159.

References

Baker, D.R., 1996. Granitic melt viscosities: Empirical and configurational entropy models for their calculation. Am. Mineral. 81, 126–134. https://doi.org/10.2138/AM-1996-1-216/PDF.

Beyreuther, M., Barsch, R., Krischer, L., et al., 2010. ObsPy: a Python Toolbox for Seismology. Seismol. Res. Lett. 81, 530–533. https://doi.org/10.1785/GSSRL.81.3.530.

Bindeman, I.N., Hudak, M.R., Palandri, J.P., et al., 2021. Rhyolitic and basaltic reference materials for TC/EA analysis: Investigation of water extraction and D/H ratios. Chem. Geol. 583, 120486 https://doi.org/10.1016/j.chemgeo.2021.120486.

Blower, J.D., Mader, H.M., Wilson, S.D.R., 2001. Coupling of viscous and diffusive controls on bubble growth during explosive volcanic eruptions. Earth Planet. Sci. Lett. 193, 47–56. https://doi.org/10.1016/S0012-821X(01)00488-5.

Blundy, J., Cashman, K., Humphreys, M., 2006. Magma heating by decompression-driven crystallization beneath andesite volcanoes. Nature 443, 76–80. https://doi.org/10.1038/nature05100.

Branney, M.J., Kokelaar, P., 1992. A reappraisal of ignimbrite emplacement: progressive aggradation and changes from particulate to non-particulate flow during emplacement of high-grade ignimbrite. Bull. Volcanol. 54, 504–520. https://doi.org/10.1007/BF00301396.

Burnham, C.W., 1964. Viscosity of a H2O rich pegmatite melt at high pressure. Geol. Soc. Am. Spec. Pap. 76, 26.

Cáceres, F., Wadsworth, F.B., Scheu, B., et al., 2020. Can nanolites enhance eruption explosivity? Geology 48, 997–1001. https://doi.org/10.1130/G47317.1.

Cáceres, F., Scheu, B., Hess, K.-U., et al., 2021. From melt to crystals: the effects of cooling on FeTi oxide nanolites crystallisation and melt polymerisation at oxidising

conditions. Chem. Geol. 563, 120057 https://doi.org/10.1016/j.chemgeo.2021.120057.
Cáceres, F., Hess, K.-U., Eitel, M., et al., 2024. Oxide nanolitisation-induced melt iron extraction causes viscosity jumps and enhanced explosivity in silicic magma. Nat. Commun. 15, 604. https://doi.org/10.1038/s41467-024-44850-x.
Casas, A.S., Wadsworth, F.B., Ayris, P.M., et al., 2019. SO2 scrubbing during percolation through rhyolitic volcanic domes. Geochim. Cosmochim. Acta. https://doi.org/10.1016/j.gca.2019.04.013.
Cassidy, M., Manga, M., Cashman, K., Bachmann, O., 2018. Controls on explosive-effusive volcanic eruption styles. Nat. Commun. 9, 2839. https://doi.org/10.1038/s41467-018-05293-3.
Castro, J.M., Dingwell, D.B., 2009. Rapid ascent of rhyolitic magma at Chaitén volcano, Chile. Nature 461, 780–783. https://doi.org/10.1038/nature08458.
Castro, J.M., Cottrell, E., Tuffen, H., et al., 2009. Spherulite crystallization induces Fe-redox redistribution in silicic melt. Chem. Geol. 268, 272–280. https://doi.org/10.1016/j.chemgeo.2009.09.006.
Castro, J.M., Cordonnier, B., Tuffen, H., et al., 2012. The role of melt-fracture degassing in defusing explosive rhyolite eruptions at volcán Chaitén. Earth Planet. Sci. Lett. 333–334, 63–69. https://doi.org/10.1016/j.epsl.2012.04.024.
Chevrel, M.O., Baratoux, D., Hess, K.-U., Dingwell, D.B., 2014. Viscous flow behavior of tholeiitic and alkaline Fe-rich martian basalts. Geochim. Cosmochim. Acta 124, 348–365. https://doi.org/10.1016/j.gca.2013.08.026.
Coats, R., Kendrick, J.E., Wallace, P.A., et al., 2018. Failure criteria for porous dome rocks and lavas: a study of Mt. Unzen, Japan. Solid Earth 9, 1299–1328. https://doi.org/10.5194/se-9-1299-2018.
Cordonnier, B., Caricchi, L., Pistone, M., et al., 2012a. The viscous-brittle transition of crystal-bearing silicic melt: Direct observation of magma rupture and healing. Geology 40, 611–614. https://doi.org/10.1130/G3914.1.
Cordonnier, B., Caricchi, L., Pistone, M., et al., 2012b. The viscous-brittle transition of crystal-bearing silicic melt: Direct observation of magma rupture and healing. Geology 40, 611–614. https://doi.org/10.1130/G3914.1.
Cordonnier, B., Schmalholz, S.M., Hess, K.U., Dingwell, D.B., 2012c. Viscous heating in silicate melts: an experimental and numerical comparison. J. Geophys. Res. Solid Earth 117, B02203. https://doi.org/10.1029/2010JB007982.
Costa, A., Melnik, O., Vedeneeva, E., 2007. Thermal effects during magma ascent in conduits. J. Geophys. Res. Solid Earth 112, B12205. https://doi.org/10.1029/2007JB004985.
Coumans, J.P.P., Llewellin, E.W.W., Wadsworth, F.B.B., et al., 2020. An experimentally validated numerical model for bubble growth in magma. J. Volcanol. Geotherm. Res. 402, 107002 https://doi.org/10.1016/j.jvolgeores.2020.107002.
Debolt, M.A., Easteal, A.J., Macedo, P.B., Moynihan, C.T., 1976. Analysis of Structural Relaxation in Glass using Rate heating Data. J. Am. Ceram. Soc. 59, 16–21. https://doi.org/10.1111/j.1151-2916.1976.tb09377.x.
Di Genova, D., A. BR, M. MH, et al., 2020. In situ observation of nanolite growth in volcanic melt: a driving force for explosive eruptions. Sci. Adv. 6, eabb0413. https://doi.org/10.1126/sciadv.abb0413.
Di Genova, D., Kolzenburg, S., Wiesmaier, S., et al., 2017. A compositional tipping point governing the mobilization and eruption style of rhyolitic magma. Nature 552, 235–238. https://doi.org/10.1038/nature24488.
Di Genova, D., Caracciolo, A., Kolzenburg, S., 2018. Measuring the degree of "nanotilization" of volcanic glasses: Understanding syn-eruptive processes recorded in melt inclusions. Lithos 318–319, 209–218. https://doi.org/10.1016/j.lithos.2018.08.011.
Dingwell, D.B., 1989. Shear viscosities of ferrosilicate liquids. Am. Mineral. 74, 1038–1044.
Dingwell, D.B., 1991. Redox viscometry of some Fe-bearing silicate melts. Am. Mineral. 76, 1560–1562.
Dingwell, D.B., Virgo, D., 1988. Viscosities of melts in the Na2OFeOFe2O3SiO2 system and factors controlling relative viscosities of fully polymerized silicate melts. Geochim. Cosmochim. Acta 52, 395–403. https://doi.org/10.1016/0016-7037(88)90095-6.
Dingwell, D.B., Webb, S.L., 1989. Structural relaxation in silicate melts and non-Newtonian melt rheology in geologic processes. Phys. Chem. Miner. 16, 508–516.
Dingwell, D.B., Romano, C., Hess, K.U., 1996. The effect of water on the viscosity of a haplogranitic melt under P-T-X conditions relevant to silicic volcanism. Contrib. Mineral. Petrol. 124, 19–28. https://doi.org/10.1007/S004100050170.
Dorfman, A., Hess, K.-U., Dingwell, D., 1996. Centrifuge-assisted falling-sphere viscometry. Eur. J. Mineral. 8, 507–514.
Eichelberger, J., 2019. Planning an International Magma Observatory. Eos (Washington DC) 100. https://doi.org/10.1029/2019eo125255.
Eichelberger, J.C., Carrigan, C.R., Westrich, H.R., Price, R.H., 1986. Non-explosive silicic volcanism. Nature 323, 598–602. https://doi.org/10.1038/323598a0.
Elders, W.A., Friðleifsson, G.Ó., Zierenberg, R.A., et al., 2011. Origin of a rhyolite that intruded a geothermal well while drilling at the Krafla volcano, Iceland. Geology 39, 231–234. https://doi.org/10.1130/G31393.1.
Fink, J.H., 1983. Structure and emplacement of a rhyolitic obsidian flow: Little Glass Mountain, Medicine Lake Highland, northern California. Geol. Soc. Am. Bull. 94, 362–380.
Foster, A., Wadsworth, F.B., Tuffen, H., et al., 2024. Evidence for the formation of silicic lava by pyroclast sintering. Nat. Commun. 15, 5347. https://doi.org/10.1038/s41467-024-49601-6.
Friðleifsson, G., … BP-P of the, 2010 undefined, 2010. Iceland Deep Drilling Project. The First IDDP Drill Hole Drilled and Completed in 2009. geothermal-energy.org, pp. 25–29.
Friedman, I., Long, W., Smith, R.L., 1963. Viscosity and water content of rhyolite glass. J. Geophys. Res. 68, 6523–6535.
Gent, A.N., 1960. Theory of the parallel plate viscometer. Br. J. Appl. Phys. 11, 85.
Giordano, D., Russell, J.K., Dingwell, D.B., 2008. Viscosity of magmatic liquids: a model. Earth Planet. Sci. Lett. 271, 123–134.
Gonnermann, H.M., Manga, M., 2003. Explosive volcanism may not be an inevitable consequence of magma fragmentation. Nature 426, 432–435.
Gottsmann, J., Giordano, D., Dingwell, D.B., 2002. Predicting shear viscosity during volcanic processes at the glass transition: a calorimetric calibration. Earth Planet. Sci. Lett. 198, 417–427. https://doi.org/10.1016/S0012-821X(02)00522-8.
Hampton, R.L., Bindeman, I.N., Stern, R.A., et al., 2021. A microanalytical oxygen isotopic and U-Th geochronologic investigation and modeling of rhyolite petrogenesis at the Krafla Central Volcano, Iceland. J. Volcanol. Geotherm. Res. 414, 107229 https://doi.org/10.1016/j.jvolgeores.2021.107229.
Hess, K.-U.U., Dingwell, D.B., 1996. Viscosities of hydrous leucogranitic melts: a non-Arrhenian model. Am. Mineral. 81, 1297–1300.
Hess, K.-U., Dingwell, D.B., Webb, S.L., 1995. The influence of excess alkalis on the viscosity of a haplogranitic melt. Am. Mineral. 80, 297–304. https://doi.org/10.2138/AM-1995-3-412.
Hess, K.-U., Cordonnier, B., Lavallée, Y., Dingwell, D.B., 2007. High-load, high-temperature deformation apparatus for synthetic and natural silicate melts. Rev. Sci. Instrum. 78, 75102–75104. https://doi.org/10.1063/1.2751398.
Hodge, I.M., 2008. A Personal Account of Developments in Enthalpy Relaxation: a Tribute to C. T. Moynihan. J. Am. Ceram. Soc. 91, 766–772. https://doi.org/10.1111/j.1551-2916.2007.02127.x.
Ilic, O., Sigmundsson, F., Lavallée, Y., et al., 2020. geological risk associated with drilling into Magma at Krafla Caldera, Iceland: preliminary evaluation. In: Proceedings World Geothermal Congress 2020.
Ingason, K., Kristjánsson, V., Einarsson, K., 2014. Design and development of the discharge system of IDDP-1. Geothermics 49, 58–65. https://doi.org/10.1016/j.geothermics.2013.05.002.
Jaupart, C., Allègre, C.J., 1991. Gas content, eruption rate and instabilities of eruption regime in silicic volcanoes. Earth Planet. Sci. Lett. 102, 413–429. https://doi.org/10.1016/0012-821X(91)90032-D.
Jónasson, K., 1994. Rhyolite volcanism in the Krafla central volcano, north-East Iceland. Bull. Volcanol. 56, 516–528. https://doi.org/10.1007/BF00302832.
Kemmer, G., Keller, S., 2010. Nonlinear least-squares data fitting in Excel spreadsheets. Nat. Protoc. 5, 267–281. https://doi.org/10.1038/nprot.2009.182.
Kenderes, S.M., Whittington, A.G., 2021. Faster geospeedometry: a Monte Carlo approach to relaxational geospeedometry for determining cooling rates of volcanic glasses. Chem. Geol. 581, 120385 https://doi.org/10.1016/j.chemgeo.2021.120385.
Kendrick, J.E., Lavallée, Y., 2022. Frictional Melting in Magma and Lava. Rev. Mineral. Geochem. 87, 919–963. https://doi.org/10.2138/rmg.2022.87.20.
Kendrick, J.E., Lavallée, Y., Hess, K.U., et al., 2013. Tracking the permeable porous network during strain-dependent magmatic flow. J. Volcanol. Geotherm. Res. 260, 117–126. https://doi.org/10.1016/j.jvolgeores.2013.05.012.
Kohlrausch, R., 1854. Theorie des elektrischen Rückstandes in der Leidener Flasche. Ann. Phys. 167, 179–214.
La Spina, G., Arzilli, F., Llewellin, E.W., et al., 2021. Explosivity of basaltic lava fountains is controlled by magma rheology, ascent rate and outgassing. Earth Planet. Sci. Lett. 553, 116658 https://doi.org/10.1016/j.epsl.2020.116658.
Lamur, A., Kendrick, J.E., Eggertsson, G.H., et al., 2017. The permeability of fractured rocks in pressurised volcanic and geothermal systems. Sci. Rep. 7, 6173. https://doi.org/10.1038/s41598-017-05460-4.
Lavallée, Y., Hess, K.-U., Cordonnier, B., Dingwell, D.B., 2007. Non-Newtonian rheological law for highly crystalline dome lavas. Geology 35, 843–846. https://doi.org/10.1130/g23594a.1.
Lavallée, Y., Meredith, P.G., Dingwell, D.B., et al., 2008. Seismogenic lavas and explosive eruption forecasting. Nature 453, 507–510. https://doi.org/10.1038/nature06980.
Lavallée, Y., Benson, P.M., Heap, M.J., et al., 2013. Reconstructing magma failure and the degassing network of domebuilding eruptions. Geology 41, 515–518. https://doi.org/10.1130/G33948.1.
Lavallée, Y., Dingwell, D.B., Johnson, J.B., et al., 2015a. Thermal vesiculation during volcanic eruptions. Nature 528, 544–547. https://doi.org/10.1038/nature16153.
Lavallée, Y., Wadsworth, F.B., Vasseur, J., et al., 2015b. Eruption and emplacement timescales of ignimbrite super-eruptions from thermo-kinetics of glass shards. Front. Earth Sci. 3, 2. https://doi.org/10.3389/feart.2015.00002.
Lavallée Y, Kendrick JE, Eichelberger JC, et al Accessing magma: a necessary revolution in Earth sciences and renewable energies. Eur Rev.
Lowenstern, J.B., Pitcher, B.W., 2013. Analysis of H2O in silicate glass using attenuated total reflectance (ATR) micro-FTIR spectroscopy‡. Am. Mineral. 98, 1660–1668. https://doi.org/10.2138/am.2013.4466.
Mader, H.M., Llewellin, E.W., Mueller, S.P., 2013. The rheology of two-phase magmas: a review and analysis. J. Volcanol. Geotherm. Res. 257, 135–158. https://doi.org/10.1016/j.jvolgeores.2013.02.014.
Maier, C.G., Kelley, K.K., 1932. An equation for the representation of high-temperature heat content data. J. Am. Chem. Soc. 54, 3243–3246. https://doi.org/10.1021/ja01347a029.
Malfait, W.J., Sanchez-Valle, C., Ardia, P., et al., 2011. Compositional dependent compressibility of dissolved water in silicate glasses, 96, 1402–1409. https://doi.org/10.2138/am.2011.3718.
Masotta, M., Mollo, S., Nazzari, M., et al., 2018. Crystallization and partial melting of rhyolite and felsite rocks at Krafla volcano: a comparative approach based on mineral and glass chemistry of natural and experimental products. Chem. Geol. 483, 603–618. https://doi.org/10.1016/j.chemgeo.2018.03.031.
Mastin, L.G., 2005. The controlling effect of viscous dissipation on magma flow in silicic conduits. J. Volcanol. Geotherm. Res. 143, 17–28. https://doi.org/10.1016/j.jvolgeores.2004.09.008.

Mortensen, A.K., Grönvold, K., Gudmundsson, Á., et al., 2010. Quenched silicic glass from well KJ-39 in Krafla, North-Eastern Iceland. In: World Geothermal Congress, pp. 1–6.
Moussallam, Y., Morizet, Y., Gaillard, F., 2016. H2O–CO2 solubility in low SiO2-melts and the unique mode of kimberlite degassing and emplacement. Earth Planet. Sci. Lett. 447, 151–160. https://doi.org/10.1016/j.epsl.2016.04.037.
Mujin, M., Nakamura, M., Miyake, A., 2017. Eruption style and crystal size distributions: Crystallization of groundmass nanolites in the 2011 Shinmoedake eruption. Am. Mineral. 102, 2367–2380. https://doi.org/10.2138/AM-2017-6052CCBYNCND.
Namiki, A., Okumura, S., Goto, A., Yamada, T., 2023. In situ observation of glass-like fragmentation of high-temperature silicate melts generating fine ashes. Commun. Earth Environ. 4, 155. https://doi.org/10.1038/s43247-023-00816-3.
Okumura, S., Uesugi, K., Goto, A., et al., 2022. Rheology of nanocrystal-bearing andesite magma and its roles in explosive volcanism. Commun. Earth Environ. 3, 241. https://doi.org/10.1038/s43247-022-00573-9.
Pálsson, B., Hólmgeirsson, S., Guðmundsson, Á., et al., 2014. Drilling of the well IDDP-1. Geothermics 49, 23–30. https://doi.org/10.1016/j.geothermics.2013.08.010.
Pereira, L., Linard, Y., Wadsworth, F.B., et al., 2024. The rheological response of magma to nanolitisation. J. Volcanol. Geotherm. Res. 108039 https://doi.org/10.1016/j.jvolgeores.2024.108039.
Persikov, E.S., Zharikov, V.A., Bukhtiyarov, P.G., 1990. The effect of volatiles on the properties of magmatic melts. Eur. J. Mineral. 621–642 https://doi.org/10.1127/EJM/2/5/0621.
Petcovic, H.L., Dufek, J.D., 2005. Modeling magma flow and cooling in dikes: Implications for emplacement of Columbia River flood basalts. J. Geophys. Res. Solid Earth 110. https://doi.org/10.1029/2004JB003432.
Pistone, M., Caricchi, L., Ulmer, P., et al., 2012. Deformation experiments of bubble- and crystal-bearing magmas: Rheological and microstructural analysis. J. Geophys. Res. Solid Earth 117. https://doi.org/10.1029/2011JB008986.
Pocklington, H.C., 1940. Rough measurement of high viscosities. Math. Proc. Camb. Philos. Soc. 36, 507–508. https://doi.org/10.1017/S0305004100017564.
Romine, W.L., Whittington, A.G., 2015. A simple model for the viscosity of rhyolites as a function of temperature, pressure and water content. Geochim. Cosmochim. Acta 170, 281–300. https://doi.org/10.1016/j.gca.2015.08.009.
Rooyakkers, S.M., Stix, J., Berlo, K., Barker, S.J., 2020. Emplacement of unusual rhyolitic to basaltic ignimbrites during collapse of a basalt-dominated caldera: the Halarauður eruption, Krafla (Iceland). GSA Bull. 132, 1881–1902. https://doi.org/10.1130/B35450.1.
Rooyakkers, S.M., Stix, J., Berlo, K., et al., 2021a. Eruption risks from covert silicic magma bodies. Geology 49, 921–925. https://doi.org/10.1130/G48697.1.
Rooyakkers, S.M., Stix, J., Berlo, K., et al., 2021b. The Origin of Rhyolitic Magmas at Krafla Central Volcano (Iceland). J. Petrol. 62 https://doi.org/10.1093/petrology/egab064.
Rule, G., 2020. The Origin of Magma Encountered during Drilling of Geothermal Well KJ-39, Krafla, Iceland and the Relationship with the Nearby IDDP-1 Magma. University of Canterbury, p. 127.
Ryan, A.G., Russell, J.K., Hess, K.-U., et al., 2015a. Vesiculation in rhyolite at low H 2 O contents: a thermodynamic model. Geochemi. Geophy. Geosyst. https://doi.org/10.1002/2015GC006024.
Ryan, A.G., Russell, J.K., Nichols, A.R.L., et al., 2015b. Experiments and models on H2O retrograde solubility in volcanic systems. Am. Mineral. 100, 774–786. https://doi.org/10.2138/AM-2015-5030.
Sæmundsson, K., Pringle, M.S., Hardarson, B.S., 2000. About the age of strata in the Krafla volcanic system. In: Proceedings of the Geoscience Society of Iceland, Spring Meeting, pp. 26–27.
Sæmundsson, K., Hjartarson, Á., Kaldal, I., et al., 2012. Geological map of the Northern volcanic zone, Iceland, Northern part. Icel Geosurvey Landsvirkjun scale 1.
Sano, K., Wada, K., Sato, E., 2015. Rates of water exsolution and magma ascent inferred from microstructures and chemical analyses of the Tokachi–Ishizawa obsidian lava, Shirataki, northern Hokkaido, Japan. J. Volcanol. Geotherm. Res. 292, 29–40. https://doi.org/10.1016/j.jvolgeores.2014.11.015.
Saubin, E., Kennedy, B., Tuffen, H., et al., 2019. Comparative field study of shallow rhyolite intrusions in Iceland: emplacement mechanisms and impact on country rocks. J. Volcanol. Geotherm. Res. 388, 106691 https://doi.org/10.1016/j.jvolgeores.2019.106691.
Saubin, E., Kennedy, B., Tuffen, H., et al., 2021. Textural and geochemical window into the IDDP-1 rhyolitic melt, Krafla, Iceland, and its reaction to drilling, 133, 1815–1830. https://doi.org/10.1130/B35598.1.
Scaillet, B., Holtz, F., Pichavant, M., Schmidt, M., 1996. Viscosity of Himalayan leucogranites: Implications for mechanisms of granitic magma ascent. J. Geophys. Res. Solid Earth 101, 27691–27699. https://doi.org/10.1029/96JB01631.
Schawe, J.E.K., Hess, K.-U., 2019. The kinetics of the glass transition of silicate glass measured by fast scanning calorimetry. Thermochim. Acta 677, 85–90.
Schulze, F., Behrens, H., Holtz, F., et al., 1996. The influence of H2O on the viscosity of a haplogranitic melt. Am. Mineral. 81, 1155–1165. https://doi.org/10.2138/AM-1996-9-1014/PDF.
Seropian, G., Kennedy, B.M., Kendrick, J.E., et al., 2022. Vesiculation of rhyolitic melts under oscillatory pressure. Front. Earth Sci. 219 https://doi.org/10.3389/FEART.2022.812311.
Shaw, H.R., 1963. Obsidian-H2O viscosities at 1000 and 2000 bars in the temperature range 700° to 900°C. J. Geophys. Res. 68, 6337–6343. https://doi.org/10.1029/JZ068i023p06337.
Sipp, A., Richet, P., 2002. Equivalence of volume, enthalpy and viscosity relaxation kinetics in glass-forming silicate liquids. J. Non-Cryst. Solids 298, 202–212. https://doi.org/10.1016/S0022-3093(02)00948-1.
Sparks, R.S.J., 1978. The dynamics of bubble formation and growth in magmas: a review and analysis. J. Volcanol. Geotherm. Res. 3, 1–37. https://doi.org/10.1016/0377-0273(78)90002-1.
Tobolsky, A.V., Taylor, R.B., 1963. Viscoelastic properties of a simple organic glass. J. Phys. Chem. 67, 2439–2442. https://doi.org/10.1021/j100805a044.
Tuffen, H., Castro, J.M., 2009. The emplacement of an obsidian dyke through thin ice: Hrafntinnuhryggur, Krafla Iceland. J. Volcanol. Geotherm. Res. 185, 352–366.
Tuffen, H., Smith, R., Sammonds, P.R., 2008. Evidence for seismogenic fracture of silicic magma. Nature 453, 511–514. https://doi.org/10.1038/nature06989.
Tuffen, H., Owen, J., Denton, J., 2010. Magma degassing during subglacial eruptions and its use to reconstruct palaeo-ice thicknesses. Earth-Sci. Rev. 99, 1–18. https://doi.org/10.1016/j.earscirev.2010.01.001.
Vasseur, J., Wadsworth, F.B., Lavallée, Y., et al., 2015. Heterogeneity: the key to failure forecasting. Sci. Rep. 5, 13259. https://doi.org/10.1038/srep13259.
Vasseur, J., Wadsworth, F.B., Dingwell, D.B., 2018. Forecasting Multiphase Magma failure at the Laboratory Scale using Acoustic Emission Data. Front. Earth Sci. 6, 132. https://doi.org/10.3389/feart.2018.00132.
Vasseur, J., Wadsworth, F.B., Dingwell, D.B., 2023. Shear thinning and brittle failure in crystal-bearing magmas arise from local non-Newtonian effects in the melt. Earth Planet. Sci. Lett. 603, 117988 https://doi.org/10.1016/j.epsl.2023.117988.
Wadsworth, F.B., Witcher, T., Vossen, C.E.J., et al., 2018. Combined effusive-explosive silicic volcanism straddles the multiphase viscous-to-brittle transition. Nat. Commun. 9, 1–8. https://doi.org/10.1038/s41467-018-07187-w.
Wadsworth, F.B., Vasseur, J., Schauroth, J., et al., 2019. A general model for welding of ash particles in volcanic systems validated using in situ X-ray tomography. Earth Planet. Sci. Lett. 525, 115726 https://doi.org/10.1016/j.epsl.2019.115726.
Wadsworth, F.B., Llewellin, E.W., Vasseur, J., et al., 2020. Explosive-effusive volcanic eruption transitions caused by sintering. Sci. Adv. 6, eaba7940. https://doi.org/10.1126/sciadv.aba7940.
Wadsworth, F., Vasseur, J., Casas, A., et al., 2021a. A model for the kinetics of high temperature reactions between polydisperse volcanic ash and SO2 gas. Am. Mineral. https://doi.org/10.2138/am-2021-7691.
Wadsworth, F.B., Vasseur, J., Llewellin, E.W., et al., 2021b. A model for permeability evolution during volcanic welding. J. Volcanol. Geotherm. Res. 409, 107118 https://doi.org/10.1016/j.jvolgeores.2020.107118.
Wadsworth, F.B, Llewellin, E., Rennie, C., et al., 2022a. Using obsidian in glass art practice. Volcanica 5, 183–207. https://doi.org/10.30909/vol.05.01.183207.
Wadsworth, F.B., Llewellin, E.W., Castro, J.M., et al., 2022b. A reappraisal of explosive–effusive silicic eruption dynamics: syn-eruptive assembly of lava from the products of cryptic fragmentation. J. Volcanol. Geotherm. Res. 107672 https://doi.org/10.1016/j.jvolgeores.2022.107672.
Wadsworth, F.B., Vasseur, J., Heap, M.J., et al., 2024. A scaling for the viscous-brittle transition in flowing crystal-bearing volcanic dome lavas with implications for the development of permeability anisotropy. J. Volcanol. Geotherm. Res. (in Rev).
Watson, T., 2018. Evolution of Magmatic Volatiles during Drilling into a Magma Body, Krafla, Iceland. University of Canterbury, p. 129.
Weaver, J., Lavallée, Y., Ashraf, M., et al., 2022. Vesiculation and densification of pyroclasts: a clast-size dependent competition between bubble growth and diffusive outgassing. J. Volcanol. Geotherm. Res. 107550 https://doi.org/10.1016/j.jvolgeores.2022.107550.
Weaver, J., Lamur, A., Lea, T.D., et al., 2023. Sintering of vesiculating pyroclasts. Earth Planet. Sci. Lett. 623, 118410 https://doi.org/10.1016/j.epsl.2023.118410.
Webb, S.L., Dingwell, D.B., 1990. Non-Newtonian rheology of igneous melts at high stresses and strain rates: Experimental results for rhyolite, andesite, basalt, and nephelinite. J. Geophys. Res. 95, 15695–15701.
Weidendorfer, D., Hess, K.-U., Ruhekenya, R.M., et al., 2023. Effect of water on the glass transition of a potassium-magnesium carbonate melt. Philos. Trans. R. Soc. A Math. Phys. Eng. Sci. 381, 20220355. https://doi.org/10.1098/rsta.2022.0355.
Westrich, H.R., Eichelberger, J.C., 1994. Gas transport and bubble collapse in rhyolitic magma: an experimental approach. Bull. Volcanol. 56, 447–458. https://doi.org/10.1007/BF00302826.
Whittington, A.G., Richet, P., Polian, A., 2012. Amorphous materials: Properties, structure, and durability. Water compressibility Silic Glas A Brillouin Spectrosc study, 97, 455–467. https://doi.org/10.2138/am.2012.3891.
Wilding, M., Webb, S., Dingwell, D.B., 1996. Tektite cooling rates: calorimetric relaxation geospeedometry applied to a natural glass. Geochim. Cosmochim. Acta 60, 1099–1103.
Williams, G., Watts, D.C., 1970. Non-symmetrical dielectric relaxation behaviour arising from a simple empirical decay function. Trans. Faraday Soc. 66, 80–85.
Wright, F.E., 1915. Obsidian from Hrafntinnuhryggur, Iceland: its lithopliysæ. And surface markings. GSA Bull. 26, 255–286. https://doi.org/10.1130/GSAB-26-255.
Yoshimura, S., Nakamura, M., 2008. Diffusive dehydration and bubble resorption during open-system degassing of rhyolitic melts. J. Volcanol. Geotherm. Res. 178, 72–80. https://doi.org/10.1016/j.jvolgeores.2008.01.017.
Zandonà, A., Scarani, A., Löschmann, J., et al., 2023. Non-stoichiometric crystal nucleation in a spodumene glass containing TiO2 as seed former: Effects on the viscosity of the residual melt. J. Non-Cryst. Solids 619, 122563. https://doi.org/10.1016/j.jnoncrysol.2023.122563.
Zierenberg, R.A., Schiffman, P., Barfod, G.H., et al., 2013. Composition and origin of rhyolite melt intersected by drilling in the Krafla geothermal field, Iceland. Contrib. Mineral. Petrol. 165, 327–347. https://doi.org/10.1007/s00410-012-0811-z.